Article

Inflammatory monocytes promote granuloma control of *Yersinia* infection

Check for updates

Daniel Sorobetea[1,3], Rina Matsuda[1,3], Stefan T. Peterson [1],
James P. Grayczyk [1], Indira Rao[1], Elise Krespan[1], Matthew Lanza[1],
Charles-Antoine Assenmacher[1], Matthias Mack [2], Daniel P. Beiting[1],
Enrico Radaelli[1] & Igor E. Brodsky [1]✉

Granulomas are organized immune cell aggregates formed in response to chronic infection or antigen persistence. The bacterial pathogen *Yersinia pseudotuberculosis* (*Yp*) blocks innate inflammatory signalling and immune defence, inducing neutrophil-rich pyogranulomas (PGs) within lymphoid tissues. Here we uncover that *Yp* also triggers PG formation within the murine intestinal mucosa. Mice lacking circulating monocytes fail to form defined PGs, have defects in neutrophil activation and succumb to *Yp* infection. *Yersinia* lacking virulence factors that target actin polymerization to block phagocytosis and reactive oxygen burst do not induce PGs, indicating that intestinal PGs form in response to *Yp* disruption of cytoskeletal dynamics. Notably, mutation of the virulence factor YopH restores PG formation and control of *Yp* in mice lacking circulating monocytes, demonstrating that monocytes override YopH-dependent blockade of innate immune defence. This work reveals an unappreciated site of *Yersinia* intestinal invasion and defines host and pathogen drivers of intestinal granuloma formation.

Microbial pathogens utilize diverse mechanisms to subvert host immunity to replicate and spread to new hosts. While acute infections can be cleared rapidly by the immune system, some pathogens evade immune defences to cause chronic disease. Chronic infections often result in formation of structures termed granulomas that limit pathogen dissemination and tissue damage[1]. Granulomas are characterized by the presence of activated phagocytes, notably monocytes and macrophages, and form in response to a wide variety of infections[2]. Monocytes are rapidly recruited to infected tissues, where they produce inflammatory cytokines and antimicrobial effector molecules, contributing to defence against multiple pathogens[3–6]. Some pathogens, however, exploit monocytes as a means of dissemination, including *Salmonella enterica*, *Yersinia pestis* and *Mycobacterium* species[7–9]. The pathogen-specific signals that induce granuloma formation remain poorly defined.

Enteropathogenic *Yersinia*, including *Y. pseudotuberculosis* (*Yp*) and *Y. enterocolitica* (*Ye*), cause self-limiting gastroenteritis and mesenteric lymphadenopathy following enteric infection[10,11]. In immune-compromised patients, however, bacteria disseminate and cause a systemic plague-like disease, indicating that the intestinal immune system is critical for control of acute infection. Indeed, the intestine constitutes a bottleneck against *Yersinia* dissemination, as bacteria in systemic organs are thought to originate predominantly from the intestinal lumen rather than gut-associated lymphoid tissues[12]. A hallmark of *Yersinia* infections is the presence of chronic pyogranulomas (PGs) in lymphoid tissue, characterized by nodular infiltrates of activated monocytes and macrophages surrounding a core of activated neutrophils[13]. Notably, the contribution of monocytes to PG formation and their role in *Yersinia* restriction are unclear[14,15].

In this Article, we report that PGs form acutely in the murine intestinal mucosa during enteric *Yersinia* infection. PGs are enriched in neutrophils and inflammatory monocytes, and contain live bacteria at levels comparable to Peyer's patches (PPs). Notably, CCR2-deficient

[1]Department of Pathobiology, School of Veterinary Medicine, University of Pennsylvania, Philadelphia, PA, USA. [2]Department of Nephrology, University Hospital Regensburg, Regensburg, Germany. [3]These authors contributed equally: Daniel Sorobetea, Rina Matsuda. ✉e-mail: ibrodsky@vet.upenn.edu

mice, which lack circulating inflammatory monocytes[16,17], form disorganized necrosuppurative lesions rather than defined PGs, are unable to contain bacteria within the lesions and succumb rapidly to infection. Moreover, mice lacking circulating monocytes exhibit reduced levels of interleukin (IL)-1 cytokines and surface expression of the neutrophil activation marker CD11b within intestinal PGs. *Yp* lacking either the virulence plasmid (pYV) encoding the type III secreted *Yersinia* Outer Proteins (Yops), or lacking Yops that block phagocytosis and the reactive oxygen burst, do not induce detectable PGs, indicating that PGs are induced in response to *Yersinia* blockade of innate immune defence. Notably, CCR2-deficient mice infected with bacteria lacking the virulence factor YopH, which blocks actin cytoskeleton dynamics, were able to restrict bacterial burdens and form defined granulomatous lesions, accompanied by restored neutrophil CD11b surface expression. Neutrophil depletion in CCR2-deficient animals abrogates control of YopH-mutant *Yersinia*, demonstrating that inflammatory monocytes overcome YopH-mediated disruption of neutrophil function. Altogether, our study identifies an unappreciated site of *Yersinia* colonization within the murine intestinal mucosa, and reveals an essential function for inflammatory monocytes in maintenance of PG architecture during *Yp* infection.

Results

Intestinal PGs form upon oral *Yersinia* infection

Yp colonizes gut-associated lymphoid tissues, resulting in acute PG formation following oral infection[18]. Interactions between *Yersinia* and immune cells within systemic tissues have been extensively documented[19–21]. In our efforts to dissect intestinal immune responses to *Yp*, we observed numerous macroscopically visible nodular lesions in the gastrointestinal tract 5 days post infection, which appeared as punctate areas of increased opacity (Fig. 1a). Lesions were most prevalent in the jejunum and ileum, ranged in number from two to over 40 in individual mice and also formed in response to *Ye* infection (Fig. 1b,c). Histology of *Yp*-infected intestines revealed focal inflammation characterized by crypt hyperplasia, oedema and submucosal to transmural cellular infiltration, whereas non-lesional areas of infected intestines appeared largely unaffected (Fig. 1d). The lesions contained infiltrates of macrophages and neutrophils surrounding colonies of coccobacilli, similar to structures that we and others observed in lymphoid tissues and have termed PGs (Fig. 1e) (refs. [15,18,22]). Consistently, flow cytometric analysis of intestinal punch biopsies containing PGs (PG+), adjacent non-granulomatous tissue (PG−), and uninfected control tissue revealed that neutrophils were the most enriched cell type within PG+ tissue, followed by macrophages and inflammatory monocytes (Fig. 1f,g). We also observed increases in eosinophils, dendritic cells and CD4+ T cells in PG+ tissue, although the relative frequencies of these populations were decreased, due to even larger increases in neutrophils, monocytes and macrophages (Extended Data Fig. 1a,b).

In lymphoid tissues, *Yp* PGs consist of a central bacterial colony, surrounded by neutrophils, which are bordered in turn by monocytes and macrophages[15,22]. Confocal microscopy demonstrated that intestinal PG also contained a central *Yp* colony surrounded by a dense population of Ly-6G+ neutrophils (Fig. 1h). Interestingly, in contrast to lymphoid tissues, CCR2+ monocytes and macrophages formed a mesh-like network of cells that both overlapped with and bordered the neutrophils (Fig. 1h). Consistent with the presence of bacterial colonies detected by histology and fluorescence microscopy, PG+ tissue harboured high numbers of viable bacteria, comparable to that found in the PPs (Fig. 1i,j). Since PPs are a major entry point and replicative niche for enteropathogenic *Yersinia* following oral innoculation[23,24], altogether, these findings reveal intestinal PGs as a previously unappreciated location of *Yersinia* invasion within the intestinal mucosa and a potential site of bacterial restriction or dissemination.
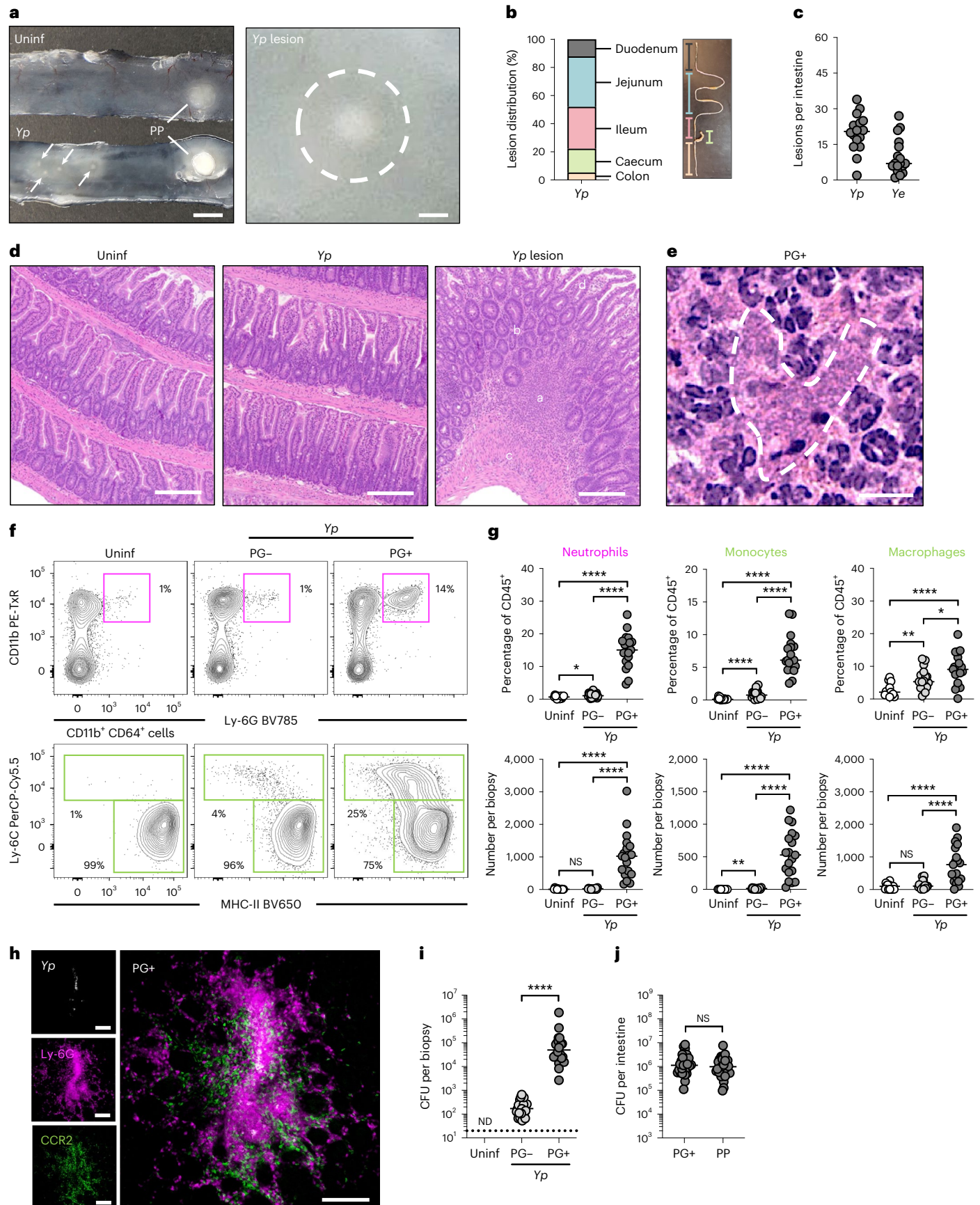
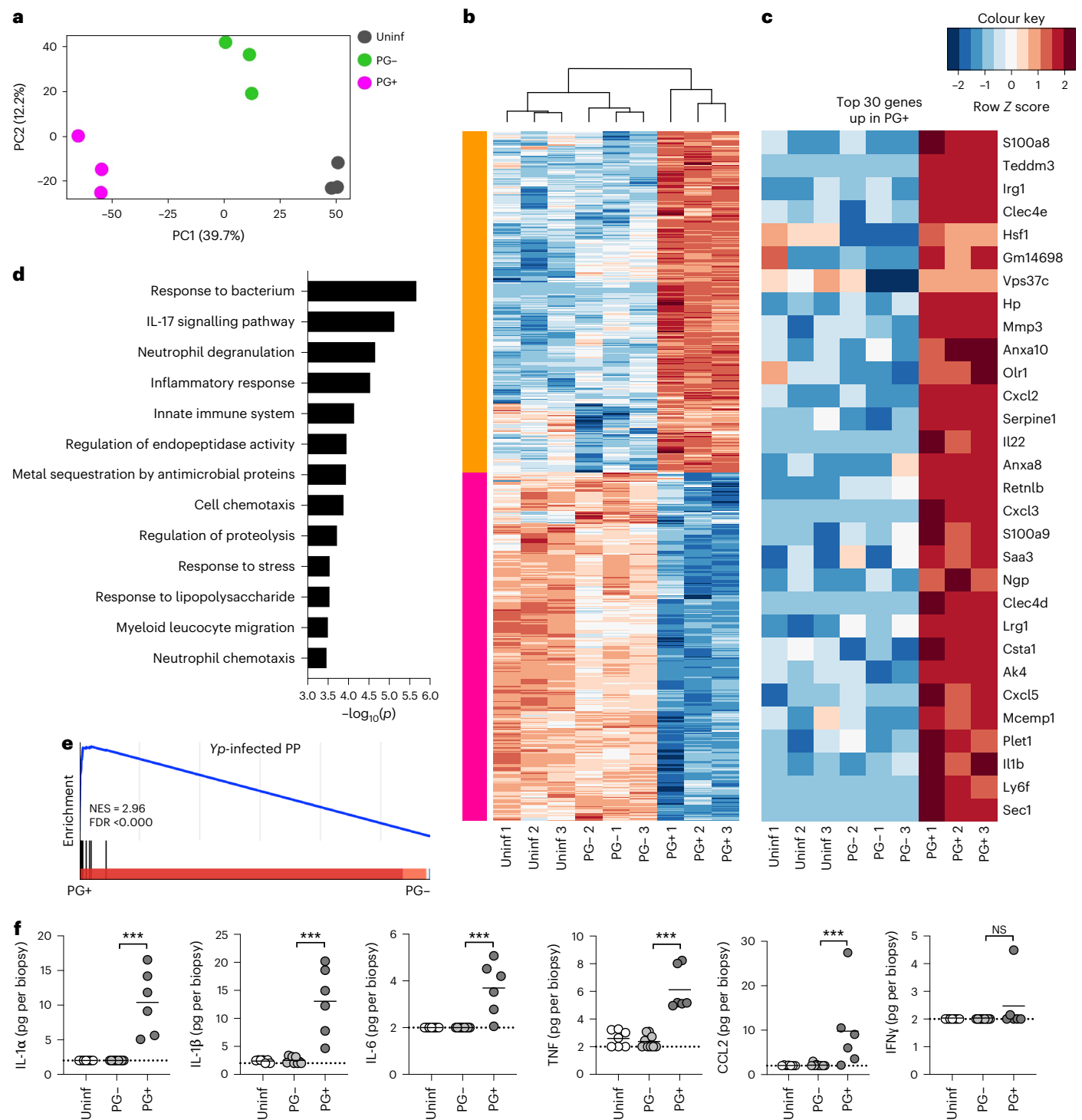### Intestinal inflammation is spatially restricted to PGs

To test whether PGs exhibit location-specific inflammatory responses, we next performed RNA sequencing of PGs, adjacent non-PG tissue and uninfected tissue. Principal component analysis showed distinct clustering by sample type (Fig. 2a), and comparison of PG+ and PG− samples revealed 355 upregulated and 363 downregulated genes (Fig. 2b). Top upregulated genes included granulocyte- and monocyte-recruiting chemokines (*Cxcl1, Cxcl2, Cxcl3 and Cxcl5*), pro-inflammatory cytokines (*Il1b and Il22*), metal-sequestration proteins (*S100a8 and S100a9*) and matrix metalloproteases (*Mmp3*) (Fig. 2c). Gene Ontology analysis indicated that chemotaxis of myeloid cells and defence against bacterial pathogens predominated the top upregulated responses within PG+ biopsies (Fig. 2d and Extended Data Table 1). These responses were strikingly similar to previously reported *Yp*-infected PPs[25]. Consistently, gene set-enrichment analysis indicated that a set of 50 upregulated genes previously reported in *Yp*-infected PPs were also enriched in PG+ samples (Fig. 2e). Furthermore, protein levels of the pro-inflammatory cytokines IL-1α, IL-1β, IL-6, TNF and and CCL2 were significantly elevated within PG+ biopsies (Fig. 2f). Consistent with histology and microscopy, the inflammatory transcriptional response was localized to PG+ tissue, as PG− samples did not exhibit enrichment of genes or ontology terms related to myeloid cell migration or innate immune-cell activation (Extended Data Fig. 2 and Extended Data Table 2). Likewise, production of pro-inflammatory cytokines was not detected in PG− tissue (Fig. 2e). Altogether, these data indicate that the pro-inflammatory response to *Yp* infection in the gut mucosa is spatially restricted to PG.

Inflammatory monocytes maintain PGs to restrict infection

Inflammatory monocytes promote host defence by differentiating into phagocytes and antigen presenting cells[4,6,26,27], producing pro-inflammatory mediators[3] and modulating other immune cell functions[5,28]. Monocyte-derived cells can also promote pathogen replication

Fig. 1 | Intestinal PGs form upon oral *Yersinia* infection. a, Small intestinal segments from uninfected (uninf) and *Yp*-infected mice with arrows depicting lesions, and a magnified lesion with dotted circle depicting size of punch biopsies. Scale bars, 3 mm (left) and 0.5 mm (right). Representative of more than three independent experiments. **b**, Frequency distribution of lesions along the intestine, with graphical key of anatomical segments. Each coloured bar represents the mean frequency of lesions in a given segment (*n* = 20 mice). Only mice with >9 total lesions (>80% of mice) were included. Pooled from three independent experiments. **c**, Quantification of total intestinal lesions at day 5 post infection with *Yp* or *Ye*. Each circle represents one mouse (*n* = 16–17). Lines represent median. Pooled from three independent experiments. **d**, H&E-stained paraffin-embedded longitudinal small-intestinal sections from uninf and *Yp*-infected mice. Scale bars, 200 μm. a is lesion, b is crypt hyperplasia, c is submucosal inflammation and d is oedema. Representative of three independent experiments. **e**, H&E-stained paraffin-embedded small-intestinal PG depicting an encircled bacterial colony. Scale bar, 10 μm. Representative of three independent experiments. **f**, Flow cytometry plots identifying CD11b+Ly-6G+ neutrophils, CD11b+CD64+Ly-6C+ monocytes and CD11b+CD64+Ly-6C−MHC-II+ macrophages in small intestinal tissue. Representative of four independent experiments. **g**, Frequency and total number of neutrophils, monocytes and macrophages in small intestinal tissue. Each circle represents one mouse (*n* = 15–19). Lines represent median. Pooled from four independent experiments. **h**, Fluorescently labelled small intestinal PG from a *Ccr2*gfp/+ mouse. White (*Yp*-mCherry), magenta (Ly-6G-AF647) and green (CCR2-GFP). Scale bars, 100 μm. Representative of two independent experiments. **i**, Bacterial burdens in small intestinal tissue. Each circle represents one mouse (*n* = 24–25). Lines represent geometric mean. Dotted line represents detection limit. Pooled from four independent experiments. **j**, Cumulative bacterial burdens in PG+ tissue and PP. Each circle represents one mouse (*n* = 29–30). Lines represent geometric mean. Pooled from five independent experiments. Wilcoxon test (two-tailed) was performed for paired analyses (PG− versus PG+). Mann–Whitney *U* test (two-tailed) was performed for remaining statistical analyses. *$P < 0.05$, **$P < 0.01$, ****$P < 0.0001$; NS, not significant; ND, not detected.

Fig. 2 | Intestinal inflammation is spatially restricted to PGs. a, Principal component analysis of PG+ (pink), PG− (green) and uninfected (uninf; grey) samples at day 5 post infection. Five biopsies were pooled per mouse. **b**, Heat map of all differentially expressed genes in PG+ compared with PG− samples. FDR <0.05 using Benjamini–Hochberg procedure. Pink and orange bars denote two clusters grouped based on Pearson correlation. **c**, Heat map of top 30 significantly upregulated genes in PG+ compared with PG− samples in descending order by fold change. FDR <0.05 using Benjamini–Hochberg procedure. **d**, Gene Ontology analysis of top 30 upregulated genes by fold change only in PG+ compared with PG− samples. p, P value. **e**, Gene set enrichment analysis of top 50 upregulated genes in *Yp*-infected PP. NES, normalized enrichment score. FDR, false discovery rate. **f**, Cytokine levels in homogenates of tissue punch biopsies at day 5 post infection. Lines represent group mean. Each circle represents one mouse ($n = 6$–9). Statistical analysis by Mann–Whitney U test (two-tailed). *$P < 0.05$, **$P < 0.01$, ***$P < 0.001$, ****$P < 0.0001$; NS, not significant. Data from one or two pooled independent experiments.

or dissemination to new sites[7,29]. Mice lacking the chemokine receptor CCR2 have a tenfold reduction in circulating monocytes due to defective bone marrow egress[16,17]. Monocytes are rapidly recruited to intestinal PGs (Fig. 1) and sites of systemic *Yp* infection[15,18,22], raising the question of their role in *Yp* infection. CCR2 deficiency has been associated with more rapid bacterial clearance from the mesenteric lymph node (MLN) following enteric *Yersinia* infection[15], but increased susceptibility to intravenous *Yp* infection[14]. Interestingly, we found that

while *Ccr2*[gfp/gfp] mice, which lack circulating monocytes due to lack of CCR2 expression[30,31], had similar overall numbers of macroscopic intestinal lesions as wild-type (WT) mice (Fig. 3a and Extended Data Fig. 3a), their lesions had a disorganized appearance, and exhibited central caseation with tissue necrosis (Fig. 3b). In contrast to WT PG that exhibited robust inflammatory infiltrates and a defined cellular organization encapsulating central bacterial colonies, *Ccr2*[gfp/gfp] intestinal lesions contained expanded coalescing bacterial colonies with limited immune cell recruitment (Fig. 3b,c). PPs of *Ccr2*[gfp/gfp] mice had similarly disorganized lesions with central tissue necrosis, suggesting that monocytes are required to establish or maintain organized PGs during *Yp* infection (Extended Data Fig. 3b). Importantly, two independent CCR2-deficient mouse lines showed significantly higher bacterial burdens in PG+ and PG− tissues compared with WT mice (Fig. 3d and Extended Data Fig. 3c). Moreover, acute depletion of monocytes in WT mice with anti-CCR2 specific antibodies resulted in increased PG− and PG+ bacterial burden (Extended Data Fig. 3d,e), demonstrating that the requirement for monocytes in control of *Yp* is not due to developmental defects in CCR2-deficient mice. Interestingly, at day 3 post infection, *Ccr2*[gfp/gfp] mice had elevated bacterial burdens in PG− tissue but not PG+ tissue, and did not exhibit overt signs of tissue necrosis in PGs (Extended Data Fig. 3f,g), indicating that the defect in bacterial control and PG architecture develops between days 3 and 5. Together, these data suggest that monocytes enable maintenance of PG architecture and restrict *Yp* within intestinal PG.

Consistent with their reduced overall cellularity, *Ccr2*[gfp/gfp] lesions exhibited decreased frequency and numbers of viable CD45+ hematopoietic cells compared with WT PG (Fig. 3e). Consistent with the important role of CCR2 in promoting monocyte egress from bone marrow[16,17], *Ccr2*[gfp/gfp] intestinal lesions contained significantly lower numbers of monocytes, macrophages and dendritic cells compared with PG from WT mice (Fig. 3e and Extended Data Fig. 4a). Notably, CCR2 deficiency did not impact T- or B-cell numbers in intestinal PGs, indicating that the defect in enteric control of *Yp* in CCR2-deficient mice was independent of adaptive immune cells (Extended Data Fig. 4a). *Ccr2*[gfp/gfp] intestinal lesions also showed a trend toward reduced neutrophil numbers (Fig. 3e), suggesting that monocytes promote recruitment, retention or survival of neutrophils within intestinal PG during *Yp* infection. This defect was specific to the intestinal lesions, as we observed similar frequencies of neutrophils in the MLN and spleen (Extended Data Fig. 4b). Immunofluorescence microscopy of the lesions indicated that neutrophils were unable to effectively contain *Yp* in the absence of monocytes, as the bacterial colony expanded outside the range of the neutrophil marker Ly-6G. This contrasted with WT PGs, in which *Yp* was fully encapsulated by neutrophils and CCR2+ cells (Fig. 3f).

Intriguingly, surface expression of the integrin CD11b, a well-established marker of neutrophil activation[32–34], was significantly reduced in both PGs and MLN of *Ccr2*[gfp/gfp] mice compared with the WT counterparts (Fig. 3g and Extended Data Fig. 4c), suggesting a defect in neutrophil activation in the absence of monocytes. CD11b is present on the neutrophil cell surface and membranes of intracellular granules, and increased CD11b surface expression occurs in inflammatory settings[35–37]. Notably, PG neutrophils in CCR2-deficient mice exhibited increased intracellular CD11b levels, suggesting that translocation of CD11b from intracellular granules to the cell surface is defective in the absence of monocytes (Extended Data Fig. 4d). Interestingly, total IL-1α and IL-1β levels were significantly reduced in *Ccr2*[gfp/gfp] PGs, whereas other pro-inflammatory cytokines were unaffected (Fig. 3h and Extended Data Fig. 4e), indicating that monocytes or monocyte-derived cells specifically produce IL-1, or promote IL-1 production by other cells within intestinal PGs. Notably, intracellular levels of IL-1 cytokines, TNF and lipocalin were unaffected in PG neutrophils in *Ccr2*[gfp/gfp] mice (Extended Data Fig. 4f), suggesting that inflammatory monocytes do not regulate neutrophil-intrinsic inflammatory cytokine and antimicrobial protein production. Altogether, these results demonstrate that inflammatory monocytes or monocyte-derived cells promote maintenance of functional granulomas that limit intestinal bacterial replication and dissemination.

Inflammatory monocytes control systemic *Yersinia*

Following systemic dissemination, *Yp* colonizes and induces PGs in lymphoid tissues[15,18,22]. Critically, both CCR2-deficient and anti-CCR2 depleted mice had significantly higher *Yp* burdens in the MLN and systemic organs (Fig. 4a and Extended Data Fig. 5a,b). Similar to intestinal tissue, systemic bacterial burdens in *Ccr2*[gfp/gfp] mice were unaffected at day 3 post infection, indicating that this defect in control develops between days 3 and 5 (Extended Data Fig. 5c). Consistent with our findings that monocytes were required for maintenance of intestinal PG architecture, infected *Ccr2*[gfp/gfp] spleens exhibited widespread tissue necrosis, free bacterial colonies and sparse immune cell recruitment, in contrast to WT spleens where neutrophils and monocytes effectively encapsulated *Yp* microcolonies within organized PGs (Fig. 4b,c). Notably, mice lacking CCR2 succumbed rapidly to acute infection (Fig. 4d and Extended Data Fig. 5d). Importantly, co-housed littermate *Ccr2*^{+/+} and *Ccr2*[gfp/+] mice were equally resistant to *Yp* infection while *Ccr2*[gfp/gfp] littermates succumbed (Fig. 4e), indicating that increased susceptibility of *Ccr2*[gfp/gfp] to *Yp* infection is not due to differences in composition of a vertically transmitted intestinal microbiota. Collectively, our findings demonstrate that inflammatory monocytes maintain organized PGs in host tissues, thereby limiting tissue necrosis and systemic bacterial dissemination, ultimately enabling bacterial control and host survival following oral *Yp* infection.

Yersinia virulence factors induce intestinal PGs

Yersinia inject Yops, which are encoded on a virulence plasmid (pYV), into target cells[38] to block phagocytosis, production of reactive oxygen species (ROS) and degranulation[20]. Interestingly, *Yp* lacking the pYV

**Fig. 3 | Inflammatory monocytes maintain PGs to restrict infection.**
a, Quantification of total intestinal lesions at day 5 post infection. Each circle represents one mouse (*n* = 20). Lines represent median. Pooled data from three independent experiments. **b**, H&E-stained small-intestinal sections from *Yp*-infected mice at day 5 post infection: 1 denotes the *Yersinia* microcolony, 2 denotes necrotic tissue. Scale bars, 250 μm (top) and 50 μm (bottom). Representative images of two independent experiments. **c**, Histopathological scores of small intestinal tissue at day 5 post infection. Each mouse was given a score between 0 and 4 (healthy to severe) for presence of bacterial colonies free from immune cell infiltrate. Each circle represents one mouse (*n* = 7–9 for uninfected (uninf) and 9–16 for *Yp*). Lines represent median. Pooled data from two independent experiments. **d**, Bacterial burdens in PG− and PG+ tissue at day 5 post infection. Each circle represents the mean *Yp*-CFU of 3–5 pooled punch biopsies from one mouse (*n* = 31–37). Lines represent geometric mean. Pooled data from six independent experiments. **e**, Total numbers and frequencies of indicated cells in small intestinal uninf, PG− and PG+ tissue at day 5 post infection. Each circle represents the mean of three to ten pooled punch biopsies from one mouse (*n* = 24). Lines represent median. Pooled data from five independent experiments. **f**, Fluorescently labelled PG+ tissue from *Yp*-infected *Ccr2*[gfp/+] (top) and *Ccr2*[gfp/gfp] (bottom) mice at day 5 post infection. Scale bars, 100 μm. Representative images of two independent experiments. **g**, PG+ neutrophil surface CD11b expression (mean fluorescent intensity, MFI) at day 5 post infection. Each circle represents the mean of three to ten pooled punch biopsies from one mouse (*n* = 6). Lines represent median. Representative of four independent experiments. **h**, Cytokine levels in homogenates of tissue punch biopsies were measured by cytometric bead array at day 5 post infection. Each circle represents the mean of three to ten pooled punch biopsies from one mouse (*n* = 18–21). Lines represent median. Pooled data from three independent experiments. Mann–Whitney *U* test (two-tailed) was performed for all statistical analyses. *$P < 0.05$, **$P < 0.01$, ***$P < 0.001$, ****$P < 0.0001$; NS, not significant.

(pYV−) still acutely colonize the intestine without causing disease[39]. Since granulomas form in response to pathogens that thwart immune defences, we hypothesized that intestinal PGs may be triggered by the activity of *Yp* effector proteins. Indeed, even at a tenfold higher infectious dose, we did not observe intestinal lesions at day 5 post infection

with pYV− bacteria (Fig. 5a), despite detectable (although reduced) intestinal colonization (Extended Data Fig. 6a).

pYV− bacteria still induced monocyte recruitment to both the intestinal mucosa and MLN, indicating that lack of detectable PG was not due to an absence of immune infiltration (Extended Data Fig. 6b).
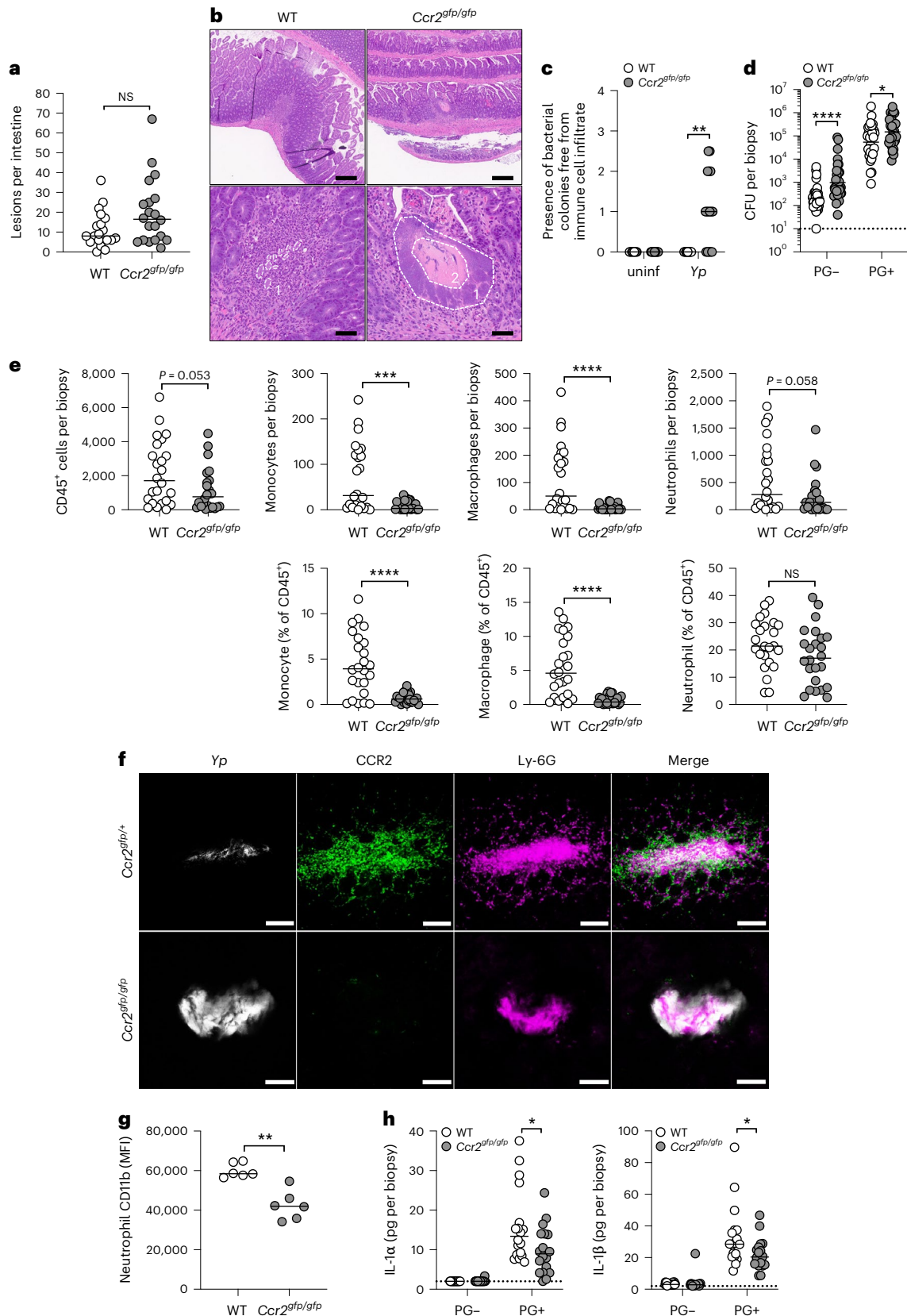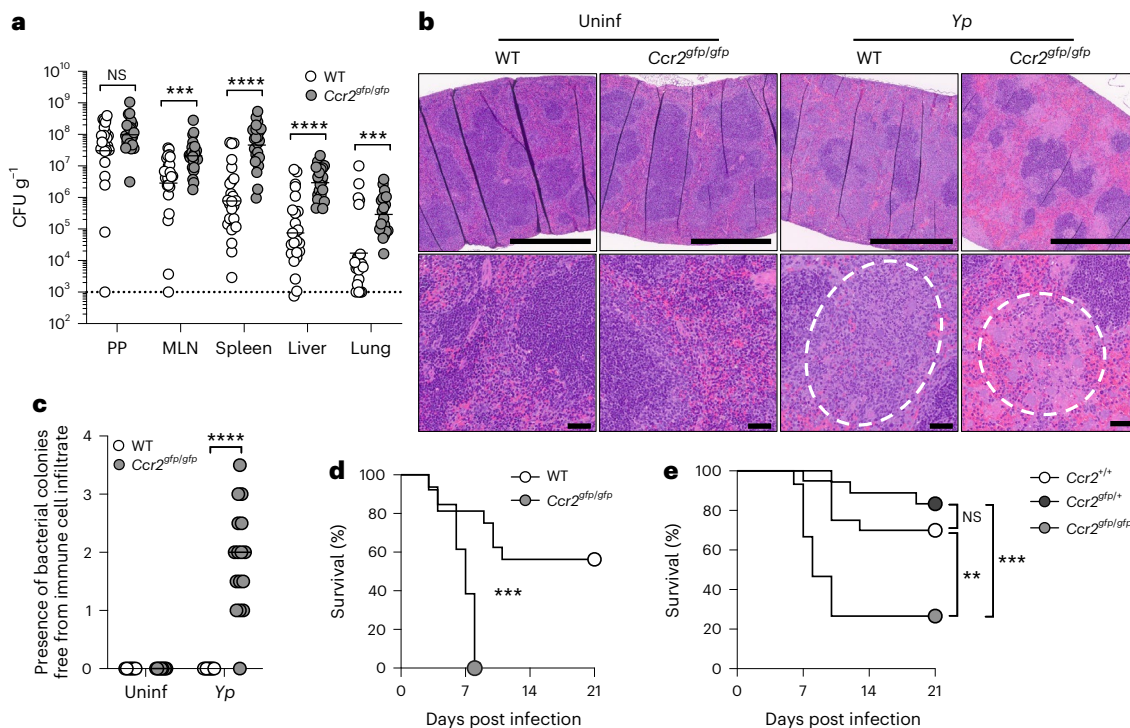
Fig. 4 | Inflammatory monocytes control systemic *Yersinia*. a, Bacterial burdens in indicated organs at day 5 post infection. Each circle represents one mouse ($n = 20-25$). Lines represent geometric mean. Pooled data from four independent experiments. **b**, H&E-stained paraffin-embedded longitudinal spleen sections from WT and *Ccr2*$^{gfp/gfp}$ mice at day 5 post infection. Dashed circle denotes area with bacterial microcolonies and neutrophils. Scale bars, 500 μm (top) and 50 μm (bottom). Representative images of two independent experiments. **c**, Histopathological scores of spleens from uninfected and *Yp*-infected mice at day 5 post infection. Each mouse was given a score between 0 and 4 (healthy–severe) for presence of bacterial colonies free from immune cell infiltrate. Each circle represents one mouse ($n = 9$ for uninfected and 16 for *Yp*). Lines represent median. Pooled data from two independent experiments. **d**, Survival of infected WT ($n = 16$) and *Ccr2*$^{gfp/gfp}$ ($n = 13$) mice. Pooled data from two independent experiments. **e**, Survival of infected littermate WT *Ccr2*$^{+/+}$ ($n = 20$), heterozygous *Ccr2*$^{gfp/+}$ ($n = 19$) and homozygous *Ccr2*$^{gfp/gfp}$ ($n = 15$) mice. Pooled data from three independent experiments. Statistical analyses by Mann–Whitney U test (two-tailed) (**a** and **c**) and Mantel–Cox test (**d** and **e**). *$P < 0.05$, **$P < 0.01$, ***$P < 0.001$, ****$P < 0.0001$; NS, not significant.

However, neutrophil accumulation was absent upon pYV− infection, demonstrating that neutrophil recruitment occurs in response to *Yp* virulence (Extended Data Fig. 6c). Although comparable in the intestinal mucosa, pYV− bacterial burdens were reduced in other gut-associated and systemic lymphoid tissues (Extended Data Fig. 6d), illustrating that intestinal PG formation is dispensable for control of pYV− *Yersinia*.

Intestinal lesions formed at WT levels in mice infected with *Yp* individually deficient in either YopM or YopJ enzymatic activity, which block pyrin inflammasome assembly or nuclear factor kappa B and mitogen-activated protein kinase signalling[40–42], respectively, suggesting that neither YopM nor YopJ is singly required for PG formation (Extended Data Fig. 6e). Several Yops function together to disrupt the actin cytoskeleton, thereby blocking phagocytosis and the reactive oxygen burst[20]. These Yops (E, H and T), have partially overlapping functions and can compensate for one another in certain settings[20]. Notably, *Yp* with combined point mutations in each of the catalytic residues of these Yops (YopE^{R144A}, YopT^{C139A} and YopH^{R409A}) did not induce intestinal lesions and had burdens similar to pYV− infection (Fig. 5a and Extended Data Fig. 6a,d). In contrast, bacteria lacking YopE and YopT, or YopE alone, induced WT numbers of intestinal lesions (Fig. 5a) and were only attenuated in systemic organs (Extended Data Fig. 6d), indicating that YopH is sufficient, in the absence of YopE and YopT, to induce PG formation. Interestingly, YopH^{R409A} mutants that lack YopH tyrosine phosphatase activity induced fewer PGs than WT bacteria (Fig. 5a), suggesting that YopH is sufficient and partially responsible for PG formation. In addition, MLN colonization was abrogated in the absence of YopH activity, whereas YopE was

dispensable for MLN colonization (Extended Data Fig. 6d). Intriguingly, bacteria lacking both YopE and YopH (*yopEH*) induced no detectable lesions (Fig. 5a) and showed similar levels of colonization to *yopETH* bacteria (Extended Data Fig. 6a,d), suggesting that the host response to YopE and YopH drives PG formation.

YopH blocks innate cell phagocytosis and ROS production[20,43–46]. YopH-deficient *Yp* are therefore more susceptible to neutrophil killing in vitro and are attenuated in vivo[47–49]. Consequently, neutrophil depletion increases susceptibility to *Yp* and restores virulence to YopH-mutant bacteria[43,45], indicating that neutrophil defences are an important target of YopH in vivo. However, whether monocytes combat YopH-dependent blockade of neutrophil function is unknown. As in WT mice, we found that YopH-mutant bacteria induced significantly fewer intestinal lesions in *Ccr2*$^{gfp/gfp}$ mice than WT bacteria (Extended Data Fig. 6f). Strikingly, despite the lack of monocytes, YopH^{R409A} infection of CCR2-deficient mice restored neutrophil recruitment and induced neutrophil-rich lesions without necrosis (Fig. 5b,c and Extended Data Fig. 6g). Intriguingly, CD11b surface expression was restored in PG+ tissue of CCR2-deficient animals infected with YopH^{R409A} bacteria, indicating that YopH limits neutrophil activation in the absence of monocytes (Fig. 5d). Furthermore, CCR2-deficient mice effectively controlled bacterial burdens in intestinal and systemic tissues following infection with YopH^{R409A} bacteria (Fig. 5e,f and Extended Data Fig. 6h). Consistently, while CCR2-deficient mice rapidly succumbed to WT *Yp*, they survived infection with YopH^{R409A} bacteria at levels similar to WT mice infected with WT *Yp*, suggesting that monocytes control *Yersinia* infection by overcoming the virulence of YopH (Fig. 5g). Altogether, these data indicate that intestinal PGs form in
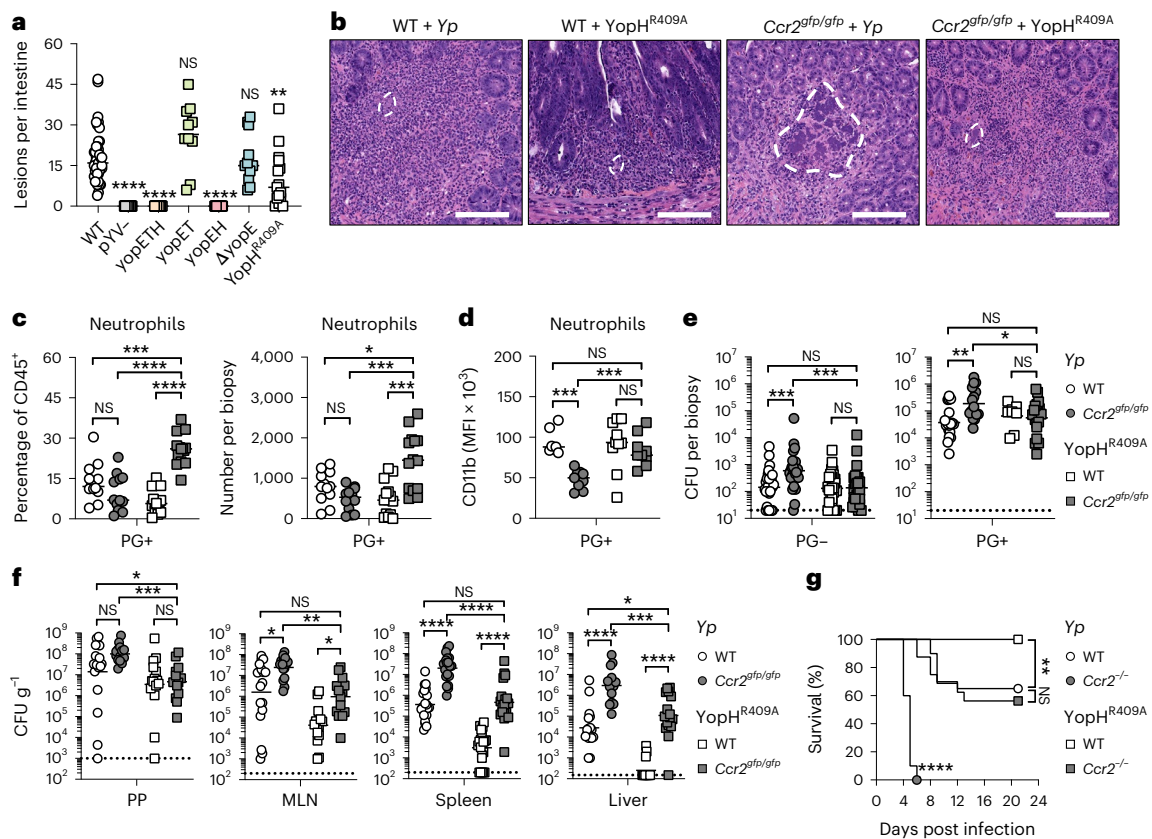
Fig. 5 | *Yersinia* virulence factors induce intestinal PGs. a, Quantification of total intestinal lesions at day 5 post *Yp* infection. Each symbol represents one mouse (*n* = 10–43). Lines represent median. Pooled from two to six independent experiments. **b**, H&E-stained paraffin-embedded transverse small-intestinal sections from WT and *Ccr2*^gfp/gfp^ mice infected with WT or YopH^R409A^ *Yp* at day 5 post infection depicting encircled bacterial colonies. Scale bars, 100 μm. Representative of two independent experiments. **c**, Frequency and total number of neutrophils in small-intestinal PG+ tissue at day 5 post WT or YopH^R409A^ *Yp* infection. Each circle represents one mouse (*n* = 12–14). Lines represent median. Pooled from three independent experiments. **d**, Mean fluorescent intensity (MFI) of surface CD11b expression on neutrophils in PG+ tissue at day 5 post WT or YopH^R409A^ *Yp* infection. Each symbol represents one mouse (*n* = 7–10). Lines

represent median. Pooled from two independent experiments. **e**, Bacterial burdens in small intestinal PG− and PG+ tissue at day 5 post WT or YopH^R409A^ *Yp* infection. Each symbol represents one mouse (*n* = 25–26). Lines represent geometric mean. Pooled from four independent experiments. **f**, Bacterial burdens in indicated organs at day 5 post WT or YopH^R409A^ *Yp* infection. Each symbol represents one mouse (*n* = 15–22). Lines represent geometric mean. Pooled from four independent experiments. **g**, Survival of WT mice infected with WT (*n* = 20) or YopH^R409A^ (*n* = 20), *Yp* and *Ccr2*^−/−^ mice infected with WT (*n* = 10) or YopH^R409A^ (*n* = 17) *Yp*. Pooled from two independent experiments. Statistical analyses by Kruskal–Wallis test with Dunn's post-test (**a** and **c**–**f**), and Mantel–Cox test (**g**). *P < 0.05, **P < 0.01, ***P < 0.001, ****P < 0.0001; NS, not significant.

response to *Yersinia* disruption of innate immune defence, and that monocytes counteract YopH activity in vivo.

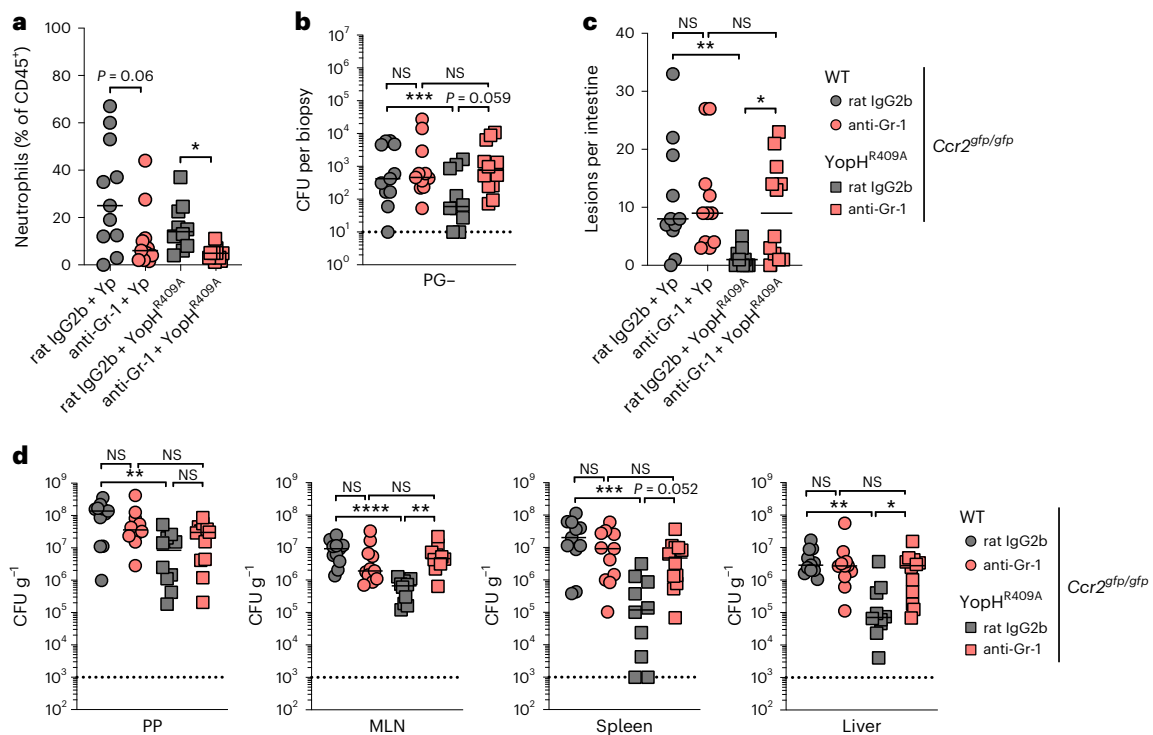## Neutrophils control YopH-deficient *Yersinia* in absence of monocytes

While monocytes are dispensable for the control of YopH-deficient *Yp*, the cell type that mediates this control in the absence of monocytes is unknown. Neutrophil recruitment to PGs was restored during infection of *Ccr2*^gfp/gfp^ mice with YopH-deficient *Yp*, raising the possibility that neutrophils mediate control of *Yersinia* in the absence of monocytes. Since *Ccr2*^gfp/gfp^ mice largely lack circulating monocytes, anti-Gr-1, which depletes both neutrophils and monocytes and is highly efficient at depleting neutrophils in infectious or inflammatory settings[50,51], allowed us to interrogate the role of neutrophils in control of YopH-mutant *Yp* (Fig. 6a and Extended Data Fig. 7a). Strikingly, *Ccr2*^gfp/gfp^ mice injected with anti-Gr-1 had elevated burdens of YopH-mutant *Yp* in PG-tissue (Fig. 6b). Anti-Gr-1 did not further reduce blood monocyte frequencies in *Ccr2*^gfp/gfp^ mice (Extended Data Fig. 7b), indicating that increased susceptibility of these mice was not attributable to depletion of remaining Ly-6C+ monocytes. CCR2-deficient mice infected with YopH^R409A^ bacteria had very few detectable PG (Fig. 6c), making it difficult to robustly analyse bacterial burdens in

this tissue. Intriguingly, *Ccr2*^gfp/gfp^ mice injected with anti-Gr-1 had elevated numbers of macroscopic intestinal lesions during infection with YopH^R409A^ bacteria (Fig. 6c). Moreover, in peripheral organs, *Ccr2*^gfp/gfp^ mice injected with anti-Gr-1 had elevated bacterial burdens following YopH-mutant infection (Fig. 6d), demonstrating that, in the absence of monocytes, neutrophils play a key role in control of YopH-deficient bacteria. Notably, mice infected with WT bacteria did not exhibit increased systemic bacterial burdens upon neutrophil depletion (Fig. 6d), consistent with effective blockade of neutrophil functions by YopH. Collectively, these data indicate that neutrophils control YopH-deficient *Yp* in the absence of monocytes.

Discussion

Granulomas are a conserved response to persistent or long-term infectious and non-infectious stimuli[1,2]. The natural rodent and human pathogen *Yp* induces formation of neutrophil-rich PGs in infected lymphoid tissues[11,13]. Here we report that PG form throughout the intestine during murine enteropathogenic *Yersinia* infection. PPs are considered the primary site of *Yersinia* intestinal infection. However, intestinal PGs harboured a similar total bacterial burden as the PPs, suggesting that PGs are a previously unrecognized niche for enteropathogenic *Yersinia* intestinal colonization. Notably,

Fig. 6 | Neutrophils control YopH-deficient *Yersinia* in absence of monocytes.
a, Frequency of neutrophils in blood at day 5 post infection was determined by flow cytometry. Each symbol represents one mouse (*n* = 10–11). Lines represent median. Pooled data from three independent experiments. **b**, Bacterial burdens in small intestinal PG− tissue at day 5 post WT or YopH[R409A] *Yp* infection. Each symbol represents one mouse (*n* = 10–12). Lines represent geometric mean. Pooled data from three independent experiments. **c**, Quantification of total number of intestinal lesions at day 5 post infection. Each symbol represents one mouse (*n* = 10–12). Lines represent median. Pooled data from three independent experiments. **d**, Bacterial burdens in indicated organs at day 5 post WT or YopH[R409A] *Yp* infection. Each symbol represents one mouse (*n* = 10–12). Lines represent geometric mean. Pooled data from three independent experiments. All statistical analyses by Kruskal–Wallis test with Dunn's post-test. *P < 0.05, **P < 0.01, ***P < 0.001, ****P < 0.0001; NS, not significant.

WT mice almost entirely restricted intestinal *Yp* and inflammation to these granulomatous foci. Interestingly, the transcriptional profile of PGs was similar to *Yp*-infected PPs[25], indicating a shared response to intestinal *Yp* infection driven by recruitment and activation of innate immune cells, which may serve to limit bacterial spread and tissue damage within the gut mucosa.

While initial formation of PGs was similar in CCR2-deficient and WT mice, monocytes were critical for maintaining architectural integrity of PGs and bacterial control in the intestine and deeper tissues during *Yersinia* infection, as monocyte deficiency was associated with widespread tissue necrosis and elevated bacterial burdens in intestinal and systemic tissues that occurred between day 3 and day 5. Interestingly, *Y. pestis*, which causes more severe disease than *Yp*, is commonly associated with necrotic and necro-suppurative lesions[52], suggesting that *Y. pestis* has evolved to overcome monocyte-mediated host defence and PG formation to enhance systemic dissemination and transmission.

Monocytes were previously reported to be dispensable for acute control of *Yp* following oral inoculation[15]. These studies employed a *Ccr2*^{−/−} mouse line[17,27] originally generated on the 129 mouse background and backcrossed to C57BL/6 (ref. [16]), raising the possibility that distinct polymorphisms in this mouse line might account for this difference. *Ccr2*[gfp/gfp] mice were generated directly on the C57BL/6 J background[30], making it unlikely that our findings are due to immunologically impactful polymorphisms that co-segregate with the *Ccr2* locus. Infection of co-housed littermates also demonstrated that susceptibility of CCR2-deficient mice is not due to differences in maternally transmitted or environmentally acquired microbiota. Additionally, acute depletion of monocytes with anti-CCR2 antibodies phenocopied CCR2-deficient mice in abrogating control of intestinal and systemic bacterial burdens, demonstrating that monocytes are critical for acute control of enteric *Yersinia* infection.

Lack of both YopE and YopH abrogated PG formation, whereas either effector alone was sufficient to induce PG formation, implying a key role for actin cytoskeleton disruption in PG formation. Notably, ablation of YopH activity alone significantly reduced numbers of intestinal PGs, indicating that YopH was predominantly responsible for PG formation. Precisely how YopH and YopE lead to PG formation remains to be determined.

Monocytes and neutrophils comprise a large proportion of Yop-injected cells in vivo[53]. YopH blocks neutrophil degranulation, ROS production, phagocytosis and release of neutrophil extracellular traps[20,43,45,49,54]. The virulence of YopH-deficient bacteria is restored upon neutrophil depletion or ROS deficiency[43,45], suggesting that YopH potently targets neutrophil function in tissues during infection. In line with these observations, PGs of CCR2-deficient mice exhibited decreased numbers of neutrophils and reduced surface expression of the activation marker CD11b, which were restored in the setting of YopH deficiency. CD11b is expressed basally on the plasma membrane and in neutrophil tertiary granules, which are recruited to the surface upon neutrophil activation[35–37,55]. Our findings imply that monocytes enhance neutrophil degranulation to overcome YopH-dependent blockade of their antimicrobial functions. Consistently, while monocytes were required for host survival in response to WT bacteria, they were dispensable for controlling YopH-mutant *Yp*. Furthermore, depletion of neutrophils in YopH[R409A]-infected CCR2-deficient mice restored bacterial virulence. Overall, our findings imply that monocytes play an important role in host defence by promoting maintenance of PG architecture and neutrophil function in the face of YopH-dependent blockade. Our study reveals a previously

unappreciated site of *Yersinia* colonization within the intestine and provides insight into granuloma formation and function during *Yersinia* infection.

Methods

Animals

C57BL/6 WT and *Ccr2*$^{gfp/gfp}$ mice[30] (in which insertion of enhanced green fluorescent protein into the translation initiation site of *Ccr2* disrupts its expression) were acquired from the Jackson Laboratory and bred at the University of Pennsylvania. *Ccr2*$^{-/-}$ mice[31] were provided by Dr Sunny Shin (University of Pennsylvania). Unless specifically noted, all animals were bred by homozygous mating and housed separately by genotype. Mice of either sex between 8 and 12 weeks of age were used for all experiments. All animal studies were performed in accordance with University of Pennsylvania Institutional Animal Care and Use Committee-approved protocols (protocol no. 804523).

Bacteria

WT *Yp* (clinical isolate strain 32777, serogroup O1) (ref. [56]) and isogenic mutants were provided by Dr James Bliska (Dartmouth College). *Ye* (strain 8081, serogroup O8)[57] was provided by Dr Stanley Falkow (Stanford University). Additional mutants lacking YopE (*ΔyopE*), enzymatic activity of YopH (YopH^{R409A}), both (denoted *yopEH*) or YopE/YopT/YopH (YopE^{R144A}T^{C139A}H^{R409A}, denoted *yopETH*) were generated by two-step allelic recombination as previously described[58] with plasmids provided by Dr James Bliska. Fluorescent *Yp* (mCherry$^+$) was generated from plasmids provided by Dr Kimberly Davis (Johns Hopkins University).

Infections

Yp and *Ye* were cultured to stationary phase at 28 °C and 250 r.p.m. shaking for 16 h in 2× YT broth supplemented with 2 µg ml^{-1} triclosan (Millipore Sigma). Mice were fasted for 16 h and subsequently inoculated by oral gavage with 100–200 µl phosphate-buffered saline (PBS). All bacterial strains were administered at 2×10^8 colony-forming units (CFU) per mouse with the exception of pYV−, *yopETH* and *yopEH*, which were administered at 2×10^9 CFU per mouse.

Antibody-mediated depletions

Mice were given daily rat IgG2 isotype control or depletion antibodies in 100 µl PBS by intraperitoneal injections from day −1 to day 4 post infection. To deplete monocytes, mice were given 20 µg rat anti-mouse CCR2 (ref. [59]) (clone MC-21 AK). To deplete neutrophils in CCR2-deficient animals, mice were given 200 µg rat anti-mouse Gr-1 (RB6-8C5; Bio X Cell).

Protein quantifications

Cytokines were measured in supernatants from homogenized tissue using Cytometric Bead Array (BD Biosciences) according to the manufacturer's instructions with the following modification: the amount of capture beads, detection reagents and sample volumes was scaled down tenfold. Data were collected on an LSRFortessa flow cytometer (BD Biosciences) with FACSDiva v9.0 (BD Biosciences) and analysed with FlowJo v10 (BD Biosciences).

Tissue preparation and cell isolation

Blood was collected by cardiac puncture upon euthanasia and collected in 250 U ml^{-1} heparin solution (Millipore Sigma) before erythrocyte lysis with Red Blood Cell Lysing Buffer (Millipore Sigma).

Lymph nodes and spleens were homogenized through a 70 µm cell strainer (Fisher Scientific), then flushed with R10 buffer consisting of Roswell Park Memorial Institute Medium 1640 (Millipore Sigma) supplemented with 10 mM HEPES (Millipore Sigma), 10% foetal bovine serum (Omega Scientific), 1 mM sodium pyruvate (Thermo Fisher Scientific) and 100 U ml^{-1} penicillin + 100 µg ml^{-1} streptomycin (Thermo Fisher Scientific).

Intestines were excised, flushed luminally with sterile PBS to remove the faeces, opened longitudinally along the mesenteric side and placed luminal side down. Small intestinal tissue containing macroscopically visible PGs (PG+), adjacent non-granulomatous areas (PG−) and uninfected control tissue (uninf) were excised using a 2 mm-ø dermal punch biopsy tool (Keyes). Biopsies within each mouse were pooled, suspended in epithelial-dissociation buffer consisting of calcium- and magnesium-free Hanks' Balanced Salt Solution (HBSS) (Thermo Fisher Scientific) supplemented with 15 mM HEPES, 10 mg ml^{-1} bovine serum albumin (BSA) (Millipore Sigma), 5 mM ethylenediaminetetraacetic acid (EDTA) (Millipore Sigma) and 100 U ml^{-1} penicillin + 100 µg ml^{-1} streptomycin, then incubated for 30 min at 37 °C under continuous agitation. To isolate immune cells from the lamina propria, the tissue was enzymatically digested in R10 buffer, along with 0.5 Wünsch units ml^{-1} liberase Thermolysin Medium (Roche), 30 µg ml^{-1} DNase I (Roche) and 5 mM CaCl$_2$ for 20 min at 37 °C under continuous agitation. The resulting cell suspensions were filtered through 100 µm cell strainers (Fisher Scientific) and subjected to density-gradient centrifugation using Percoll (GE Healthcare). Briefly, cells were suspended in 40% Percoll and centrifuged over a 70% Percoll layer for 20 min at 600g, with lowest brake at room temperature. Cells collected between the layers were washed with R10 for downstream analysis.

Flow cytometry

Unspecific constant fragment (Fc) binding was blocked for 10 min on ice with anti-CD16/CD32 (93; Thermo Fisher Scientific). Cells were subsequently stained for 30 minutes on ice with the following antibodies and reagents: PE-conjugated rat anti-mouse Siglec-F (E50-2440; BD Biosciences), PE-TxR or PE-Cy5-conjugated rat anti-mouse CD11b (M1/70.15; Thermo Fisher Scientific), PE-Cy5-conjugated mouse anti-mouse NK1.1 (PK136; BioLegend), PE-Cy5.5 or PE-Cy7-conjugated rat anti-mouse CD4 (RM4-5; Thermo Fisher Scientific), PE-Cy7-conjugated rat anti-mouse CD3 (17A2; BioLegend), BV510-conjugated rat anti-mouse CD3e (145-2C11; BioLegend), FITC-conjugated Armenian hamster anti-mouse CD11c (N418; BioLegend), PerCP-Cy5.5-conjugated rat anti-mouse Ly-6C (HK1.4; Thermo Fisher Scientific), PB-conjugated rat anti-mouse CD90.2 (53-2.1; BioLegend), BV510-conjugated rat anti-mouse CD19 (1D3; BD Biosciences), BV605-conjugated Armenian hamster anti-mouse TCRβ (H57-597; BD Biosciences), BV650-conjugated rat anti-mouse I-A/I-E (M5/114.15.2; BD Biosciences), BV711-conjugated rat anti-mouse CD8α (53-6.7; BD Biosciences), BV785-conjugated rat anti-mouse Ly-6G (1A8; Thermo Fisher Scientific), AF647-conjugated mouse anti-mouse CD64 (X54-5/7.1; BD Biosciences), AF700-conjugated mouse anti-mouse CD45.2 (104; BioLegend) and PE-CF594-conjugated rat anti-mouse CD45R/B220 (RA3-6B2; BD Biosciences) along with eF780 viability dye (BioLegend) diluted in PBS. Antibodies were used at 1:200 dilution and viability dye at 1:1,500 dilution.

For intracellular staining, cells were incubated for 3 h at 37 °C with 5% CO$_2$ in R10 buffer supplemented with 0.33 µl ml^{-1} GolgiStop (BD Biosciences) and 15 µg ml^{-1} DNase I. Surface proteins were stained as above, then cells were fixed for 20 min on ice with Cytofix/Cytoperm Fixation/Permeabilization solution (BD Biosciences). Lipocalin-2 was stained using biotin-conjugated rat anti-mouse lipocalin-2 (NGAL; BioLegend) on ice for 1 h followed by BV711-conjugated streptavidin (BD Biosciences) at 4 °C overnight. Intracellular cytokines were stained at 4 °C overnight with PerCP-e710-conjugated rat anti-mouse IL-1β (NJTEN3; Thermo Fisher Scientific), eF450-conjugated rat anti-mouse TNF (MP6-XT22; Thermo Fisher Scientific) and PE-conjugated Armenian hamster anti-mouse IL-1α (ALF-161; BioLegend). All intracellular antibodies were diluted 1:200 in Perm/Wash Buffer (BD Biosciences). Streptavidin was diluted 1:400 in Perm/Wash Buffer. Cells were acquired on an LSRFortessa flow cytometer with FACSDiva v9.0, and data were analysed with FlowJo v10. Dead and clustered cells were removed from all analyses.

Histology

Tissues were fixed in 10% neutral-buffered formalin (Fisher Scientific) and stored at 4 °C until further processing. Tissue pieces were embedded in paraffin, sectioned by standard histological techniques and stained with hematoxylin and eosin (H&E) for subsequent histopathological disease scoring by blinded board-certified pathologists. Tissue sections were given scores between 0 and 4 (healthy to severe) for multiple parameters, including degree of inflammatory cell infiltration, necrosis and free bacterial colonies along with tissue-specific parameters such as villus blunting and crypt hyperplasia. Healthy mice were characterized by and subsequently scored as having none or low levels of the parameters described, whereas severely afflicted mice presented with high amounts of the respective parameters.

Fluorescence microscopy

Small intestinal tissue was dissected and flushed with PBS. Intestines were opened longitudinally and ~0.5 cm tissue pieces containing macroscopically visible lesions were excised. Tissues were fixed in 1% paraformaldehyde overnight, then blocked for 2 h at room temperature in blocking solution containing 10% bovine serum albumin, 1 μg ml^{-1} anti-CD16/32 and 0.5% normal rat IgG in PBS. AF647-conjugated anti-Ly-6G antibody (1A8; BioLegend) was added at 0.01 mg ml^{-1} in 100 μl PBS per sample, then whole tissue was stained for 24 h at 4 °C. Samples were washed three times with PBS, mounted whole onto slides in Prolong Glass Antifade Mountant (Thermo Fisher Scientific) and cured for 2 days at room temperature. Images were acquired on a DMI 6000 laser-scanning confocal microscope (Leica) with a 20× NA 0.75 oil-immersion objective. The centre of the sample was determined in the Z direction, then imaged.

Images were analysed using ImageJ v2.1. Adjustments for brightness and contrast were applied to the entire image. No threshold manipulation was performed. Green and magenta channels were pseudo-coloured.

RNA sequencing

Intestinal punch biopsies were collected as described above. Five biopsies per sample type were pooled for each mouse. RNA was extracted using the RNeasy Plus Mini Kit (Qiagen). Sequence-ready libraries were prepared using the Illumina TruSeq Stranded Total RNA kit with Ribo-Zero Gold rRNA depletion (Illumina). Quality assessment and quantification of RNA preparations and libraries were carried out using an Agilent 4200 TapeStation and Qubit 3, respectively. Samples were sequenced on an Illumina NextSeq 500 to produce 150 bp single-end reads with a mean sequencing depth of 9 million reads per sample. Raw reads from this study were mapped to the mouse reference transcriptome (Ensembl; *Mus musculus* GRCm38) using Kallisto v0.46.2 (ref. [60]). Raw sequence data are available on the Gene Expression Omnibus (GEO; accession no. GSE194334).

All subsequent analyses were carried out using the statistical computing environment R v4.0.3 in RStudio v1.2.5042 and Bioconductor[61]. Briefly, transcript quantification data were summarized to genes using the tximport package[62] and normalized using the trimmed mean of M values method in edgeR[63]. Genes with <1 counts per million (CPM) in three samples were filtered out. Normalized filtered data were variance stabilized using the voom function in limma[64], and differentially expressed genes were identified with linear modelling using limma (false discovery rate (FDR) ≤0.05; absolute log$_2$fold change ≥1) after correcting for multiple testing using Benjamini–Hochberg.

Statistics

Statistical analyses were performed using Prism v9.0 (GraphPad Software). Independent groups were compared by Mann–Whitney U test or Kruskal–Wallis test with Dunn's multiple comparisons test. Survival curves were compared by Mantel–Cox test. Statistical significance is denoted as $*P < 0.05$, $**P < 0.01$, $***P < 0.001$, $****P < 0.0001$ or NS (not significant, $P > 0.05$).

Reporting summary

Further information on research design is available in the Nature Portfolio Reporting Summary linked to this article.

Data availability

Raw RNA sequencing data are available on the Gene Expression Omnibus (accession no. GSE194334). All other raw data are available upon request to the corresponding author.

Code availability

Code for RNA sequencing analysis is available in the Supplementary Code File.

References

1. Pagán, A. J. & Ramakrishnan, L. The formation and function of granulomas. *Annu. Rev. Immunol.* **36**, 639–665 (2018).
2. Petersen, H. J. & Smith, A. M. The role of the innate immune system in granulomatous disorders. *Front. Immunol.* **4**, 1–11 (2013).
3. Casson, C. N. et al. Neutrophils and Ly6Chi monocytes collaborate in generating an optimal cytokine response that protects against pulmonary *Legionella pneumophila* infection. *PLoS Pathog.* **13**, e1006309 (2017).
4. Dunay, I. R. et al. Gr1+ inflammatory monocytes are required for mucosal resistance to the pathogen *Toxoplasma gondii*. *Immunity* **29**, 306–317 (2008).
5. Espinosa, V. et al. Inflammatory monocytes orchestrate innate antifungal immunity in the lung. *PLoS Pathog.* **10**, e1003940 (2014).
6. Seo, S.-U. et al. Intestinal macrophages arising from CCR2$^+$ monocytes control pathogen infection by activating innate lymphoid cells. *Nat. Commun.* **6**, 8010 (2015).
7. Antonelli, L. R. et al. Intranasal Poly-IC treatment exacerbates tuberculosis in mice through the pulmonary recruitment of a pathogen-permissive monocyte/macrophage population. *J. Clin. Invest.* **120**, 1674–1682 (2010).
8. St. John, A. L. et al. S1P-dependent trafficking of intracellular *Yersinia pestis* through lymph nodes establishes buboes and systemic infection. *Immunity* **41**, 440–450 (2014).
9. Eisele, N. A. et al. Salmonella require the fatty acid regulator PPARδ for the establishment of a metabolic environment essential for long term persistence. *Cell Host Microbe* **14**, 171–182 (2013).
10. Paff, J. R., Triplett, D. A. & Saari, T. N. Clinical and laboratory aspects of *Yersinia pseudotuberculosis* infections, with a report of two cases. *Am. J. Clin. Pathol.* **66**, 101–110 (1976).
11. El-Maraghi, N. R. H. & Mair, N. S. The histopathology of enteric infection with *Yersinia pseudotuberculosis*. *Am. J. Clin. Pathol.* **71**, 631–639 (1979).
12. Barnes, P. D., Bergman, M. A., Mecsas, J. C. & Isberg, R. R. *Yersinia pseudotuberculosis* disseminates directly from a replicating bacterial pool in the intestine. *J. Exp. Med.* **203**, 1591–1601 (2006).
13. Lamps, L. W. et al. The role of *Yersinia enterocolitica* and *Yersinia pseudotuberculosis* in granulomatous appendicitis: a histologic and molecular study. *Am. J. Surg. Pathol.* **25**, 508–515 (2001).
14. Zhang, Y., Tam, J. W., Mena, P., van der Velden, A. W. M. & Bliska, J. B. CCR2$^+$ inflammatory dendritic cells and translocation of antigen by type III secretion are required for the exceptionally large CD8$^+$ T cell response to the protective YopE69-77 epitope during *Yersinia* infection. *PLoS Pathog.* **11**, e1005167 (2015).
15. Zhang, Y., Khairallah, C., Sheridan, B. S., van der Velden, A. W. M. & Bliska, J. B. CCR2$^+$ inflammatory monocytes are recruited to *Yersinia pseudotuberculosis* pyogranulomas and dictate adaptive responses at the expense of innate immunity during oral infection. *Infect. Immun.* **86**, e00782–17 (2018).

16. Kuziel, W. A. et al. Severe reduction in leukocyte adhesion and monocyte extravasation in mice deficient in CC chemokine receptor 2. *Proc. Natl Acad. Sci. USA* **94**, 12053–12058 (1997).

17. Serbina, N. V. & Pamer, E. G. Monocyte emigration from bone marrow during bacterial infection requires signals mediated by chemokine receptor CCR2. *Nat. Immunol.* **7**, 311–317 (2006).

18. Peterson, L. W. et al. RIPK1-dependent apoptosis bypasses pathogen blockade of innate signaling to promote immune defense. *J. Exp. Med.* **214**, 3171–3182 (2017).

19. Tsutomu, U. Studies on the pathogenicity of *Yersinia enterocolitica* III. Comparative studies between *Y. enterocolitica* and *Y. pseudotuberculosis*. *Microbiol. Immunol.* **21**, 505–516 (1977).

20. Bliska, J. B., Brodsky, I. E. & Mecsas, J. Role of the *Yersinia pseudotuberculosis* virulence plasmid in pathogen-phagocyte interactions in mesenteric lymph nodes. *EcoSal* **9**, eESP-0014–eESP-2021 (2021).

21. Davis, K. M. All *Yersinia* are not created equal: phenotypic adaptation to distinct niches within mammalian tissues. *Front. Cell. Infect. Microbiol.* **8**, 1–8 (2018).

22. Davis, K. M., Mohammadi, S. & Isberg, R. R. Community behavior and spatial regulation within a bacterial microcolony in deep tissue sites serves to protect against host attack. *Cell Host Microbe* **17**, 21–31 (2015).

23. Clark, M. A., Hirst, B. H. & Jepson, M. A. M-cell surface β1 integrin expression and invasin-mediated targeting of *Yersinia* pseudotuberculosis to mouse Peyer's patch M cells. *Infect. Immun.* **66**, 1237–1243 (1998).

24. Fasciano, A. C. et al. *Yersinia pseudotuberculosis* YopE prevents uptake by M cells and instigates M cell extrusion in human ileal enteroid-derived monolayers. *Gut Microbes* **13**, 1988390 (2021).

25. Nuss, A. M. et al. Tissue dual RNA-seq allows fast discovery of infection-specific functions and riboregulators shaping host-pathogen transcriptomes. *Proc. Natl Acad. Sci. USA* **114**, E791–E800 (2017).

26. Serbina, N. V., Salazar-Mather, T. P., Biron, C. A., Kuziel, W. A. & Pamer, E. G. TNF/iNOS-producing dendritic cells mediate innate immune defense against bacterial infection. *Immunity* **19**, 59–70 (2003).

27. Zigmond, E. et al. Ly6C hi monocytes in the inflamed colon give rise to proinflammatory effector cells and migratory antigen-presenting cells. *Immunity* **37**, 1076–1090 (2012).

28. Grainger, J. R. et al. Inflammatory monocytes regulate pathologic responses to commensals during acute gastrointestinal infection. *Nat. Med.* **19**, 713–721 (2013).

29. Davis, J. M. & Ramakrishnan, L. The role of the granuloma in expansion and dissemination of early tuberculous infection. *Cell* **136**, 37–49 (2009).

30. Satpathy, A. T. et al. Notch2-dependent classical dendritic cells orchestrate intestinal immunity to attaching-and-effacing bacterial pathogens. *Nat. Immunol.* **14**, 937–948 (2013).

31. Boring, L. et al. Impaired monocyte migration and reduced type 1 (Th1) cytokine responses in C-C chemokine receptor 2 knockout mice. *J. Clin. Invest.* **100**, 2552–2561 (1997).

32. Borjesson, D. L., Simon, S. I., Hodzic, E., Ballantyne, C. M. & Barthold, S. W. Kinetics of CD11b/CD18 up-regulation during infection with the agent of human granulocytic ehrlichiosis in mice. *Lab. Investig.* **82**, 303–311 (2002).

33. Mann, B. S. & Chung, K. F. Blood neutrophil activation markers in severe asthma: lack of inhibition by prednisolone therapy. *Respir. Res.* **7**, 1–10 (2006).

34. Yoon, J. W., Pahl, M. V. & Vaziri, N. D. Spontaneous leukocyte activation and oxygen-free radical generation in end-stage renal disease. *Kidney Int.* **71**, 167–172 (2007).

35. Othman, A., Sekheri, M. & Filep, J. G. Roles of neutrophil granule proteins in orchestrating inflammation and immunity. *FEBS J.* **289**, 3932–3953 (2022).

36. Rijneveld, A. W., De Vos, A. F., Florquin, S., Verbeek, J. S. & van der Poll, T. CD11b limits bacterial outgrowth and dissemination during murine pneumococcal pneumonia. *J. Infect. Dis.* **191**, 1755–1760 (2005).

37. Latger-Cannard, V., Besson, I., Doco-Lecompte, T. & Lecompte, T. A standardized procedure for quantitation of CD11b on polymorphonuclear neutrophil by flow cytometry: potential application in infectious diseases. *Clin. Lab. Haematol.* **26**, 177–186 (2004).

38. Portnoy, D. A., Wolf-Watz, H., Bolin, I., Beeder, A. B. & Falkow, S. Characterization of common virulence plasmids in yersinia species and their role in the expression of outer membrane proteins. *Infect. Immun.* **43**, 108–114 (1984).

39. Balada-Llasat, J. M. & Mecsas, J. C. *Yersinia* has a tropism for B and T cell zones of lymph nodes that is independent of the type III secretion system. *PLoS Pathog.* **2**, e86 (2006).

40. Mukherjee, S. et al. *Yersinia* YopJ acetylates and inhibits kinase activation by blocking phosphorylation. *Science* **312**, 1211–1214 (2006).

41. Brodsky, I. E. & Medzhitov, R. Reduced secretion of YopJ by *Yersinia* limits in vivo cell death but enhances bacterial virulence. *PLoS Pathog.* **4**, e1000067 (2008).

42. Chung, L. K. et al. The *Yersinia virulence* factor yopm hijacks host kinases to inhibit type III effector-triggered activation of the pyrin inflammasome. *Cell Host Microbe* **20**, 296–306 (2016).

43. Rolán, H. G., Durand, E. A. & Mecsas, J. Identifying *Yersinia* YopH-targeted signal transduction pathways that impair neutrophil responses during in vivo murine infection. *Cell Host Microbe* **14**, 306–317 (2013).

44. Green, S. P., Hartland, E. L., Robins-Browne, R. M. & Phillips, W. A. Role of YopH in the suppression of tyrosine phosphorylation and respiratory burst activity in murine macrophages infected with *Yersinia enterocolitica*. *J. Leukoc. Biol.* **57**, 972–977 (1995).

45. Shaban, L. et al. *Yersinia pseudotuberculosis* YopH targets SKAP2-dependent and independent signaling pathways to block neutrophil antimicrobial mechanisms during infection. *PLoS Pathog.* **16**, e1008576 (2020).

46. Mecsas, J., Raupach, B. & Falkow, S. The *Yersinia* Yops inhibit invasion of *Listeria*, *Shigella* and *Edwardsiella* but not *Salmonella* into epithelial cells. *Mol. Microbiol.* **28**, 1269–1281 (1998).

47. Logsdon, L. K. & Mecsas, J. C. Requirement of the *Yersinia pseudotuberculosis* effectors YopH and YopE in colonization and persistence in intestinal and lymph tissues. *Infect. Immun.* **71**, 4595–4607 (2003).

48. Fisher, M. L., Castillo, C. & Mecsas, J. Intranasal inoculation of mice with *Yersinia pseudotuberculosis* causes a lethal lung infection that is dependent on *Yersinia* Outer Proteins and PhoP. *Infect. Immun.* **75**, 429–442 (2007).

49. Westermark, L., Fahlgren, A. & Fällman, M. *Yersinia pseudotuberculosis* efficiently escapes polymorphonuclear neutrophils during early infection. *Infect. Immun.* **82**, 1181–1191 (2014).

50. Stackowicz, J., Jönsson, F. & Reber, L. L. Mouse models and tools for the in vivo study of neutrophils. *Front. Immunol.* **10**, 3130 (2020).

51. Wojtasiak, M. et al. Depletion of Gr-1+, but not Ly6G+, immune cells exacerbates virus replication and disease in an intranasal model of herpes simplex virus type 1 infection. *J. Gen. Virol.* **91**, 2158–2166 (2010).

52. Bozue, J. et al. A *Yersinia pestis* tat mutant is attenuated in bubonic and small-aerosol pneumonic challenge models of infection but not as attenuated by intranasal challenge. *PLoS ONE* **9**, e104524 (2014).

53. Durand, E. A., Maldonado-Arocho, F. J., Castillo, C., Walsh, R. L. & Mecsas, J. C. The presence of professional phagocytes dictates the number of host cells targeted for Yop translocation during infection. *Cell. Microbiol.* **12**, 1064–1082 (2010).

54. Taheri, N., Fahlgren, A. & Fällman, M. *Yersinia pseudotuberculosis* blocks neutrophil degranulation. *Infect. Immun.* **84**, 3369–3378 (2016).

55. Murphy, A. J. et al. Neutrophil activation is attenuated by high-density lipoprotein and apolipoprotein A-I in in vitro and in vivo models of inflammation. *Arterioscler. Thromb. Vasc. Biol.* **31**, 1333–1341 (2011).

56. Simonet, M. & Falkow, S. Invasin expression in *Yersinia pseudotuberculosis*. *Infect. Immun.* **60**, 4414–4417 (1992).

57. Portnoy, D. A., Moseley, S. L. & Falkow, S. Characterization of plasmids and plasmid-associated determinants of *Yersinia enterocolitica* pathogenesis. *Infect. Immun.* **31**, 775–782 (1981).

58. Zhang, Y., Murtha, J., Roberts, M. A., Siegel, R. M. & Bliska, J. B. Type III secretion decreases bacterial and host survival following phagocytosis of *Yersinia pseudotuberculosis* by macrophages. *Infect. Immun.* **76**, 4299–4310 (2008).

59. Mack, M. et al. Expression and characterization of the chemokine receptors CCR2 and CCR5 in mice. *J. Immunol.* **166**, 4697–4704 (2001).

60. Bray, N. L., Pimentel, H., Melsted, P. & Pachter, L. Near-optimal probabilistic RNA-seq quantification. *Nat. Biotechnol.* **34**, 525–527 (2016).

61. Huber, W. et al. Orchestrating high-throughput genomic analysis with Bioconductor. *Nat. Methods* **12**, 115–121 (2015).

62. Soneson, C., Love, M. I. & Robinson, M. D. Differential analyses for RNA-seq: transcript-level estimates improve gene-level inferences. *F1000Research* **4**, 1521 (2016).

63. Robinson, M. D., McCarthy, D. J. & Smyth, G. K. edgeR: a Bioconductor package for differential expression analysis of digital gene expression data. *Bioinformatics* **26**, 139–140 (2010).

64. Ritchie, M. E. et al. limma powers differential expression analyses for RNA-sequencing and microarray studies. *Nucleic Acids Res.* **43**, e47 (2015).

Author contributions

D.S. established the initial findings of intestinal granulomas. D.S., R.M. and I.E.B. conceptualized the study and devised experiments. D.S. and R.M. devised the methodology and performed experiments. S.T.P., J.P.G. and I.R. performed experiments. C.-A.A., E.R. and M.L. performed the histology and histopathological scoring. E.K. prepared the RNA sequencing libraries. M.M. provided the anti-CCR2 antibody. R.M. and D.B. analysed the RNA sequencing data. I.E.B. acquired the funding and supervised the study. D.S., R.M. and I.E.B. wrote the original draft. All authors reviewed and edited the manuscript.

Competing interests

The authors declare no competing interests.

Additional information

Extended data is available for this paper at https://doi.org/10.1038/s41564-023-01338-6.

Supplementary information The online version contains supplementary material available at https://doi.org/10.1038/s41564-023-01338-6.

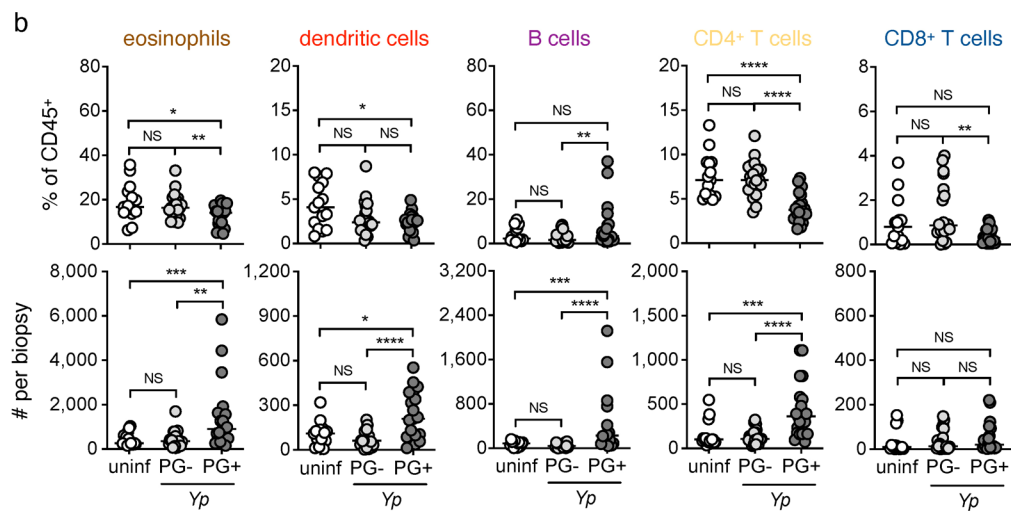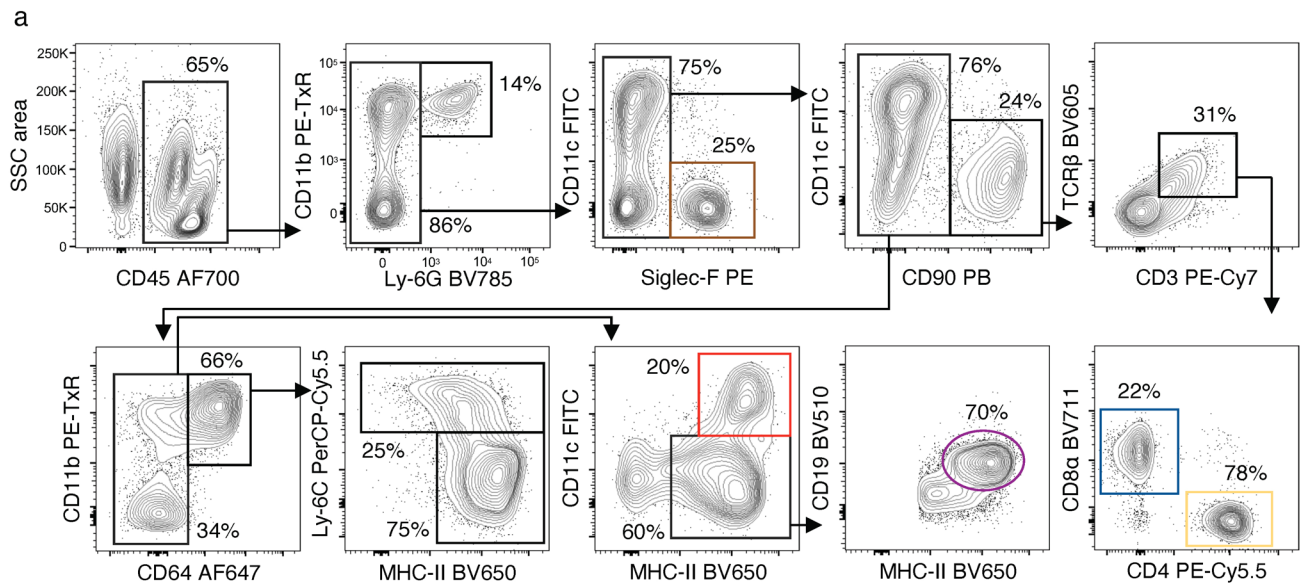**Correspondence and requests for materials** should be addressed to Igor E. Brodsky.

Peer review information *Nature Microbiology* thanks the anonymous reviewers for their contribution to the peer review of this work.

Reprints and permissions information is available at www.nature.com/reprints.

Extended Data Fig. 1 | Intestinal pyogranulomas form upon oral *Yersinia* infection. (**a**) Flow cytometry plots displaying the gating strategy employed to identify eosinophils, dendritic cells, B cells and T cells in small-intestinal tissue at day 5 post-Yp infection. Representative of four independent experiments. (**b**) Frequency and total number of eosinophils, dendritic cells, B cells, CD4+ T cells and CD8+ T cells in small-intestinal tissue at day 5 post *Yp*-infection. Each data point represents one mouse (n = 15-20). Lines represent median. Pooled from four independent experiments. Wilcoxon test (two-tailed) was performed for paired analyses (PG- vs PG +). Mann-Whitney U test (two-tailed) was performed for all remaining statistical analyses. * (p < 0.05), ** (p < 0.01), *** (p < 0.001), **** (p < 0.0001), NS (not significant, p > 0.05).
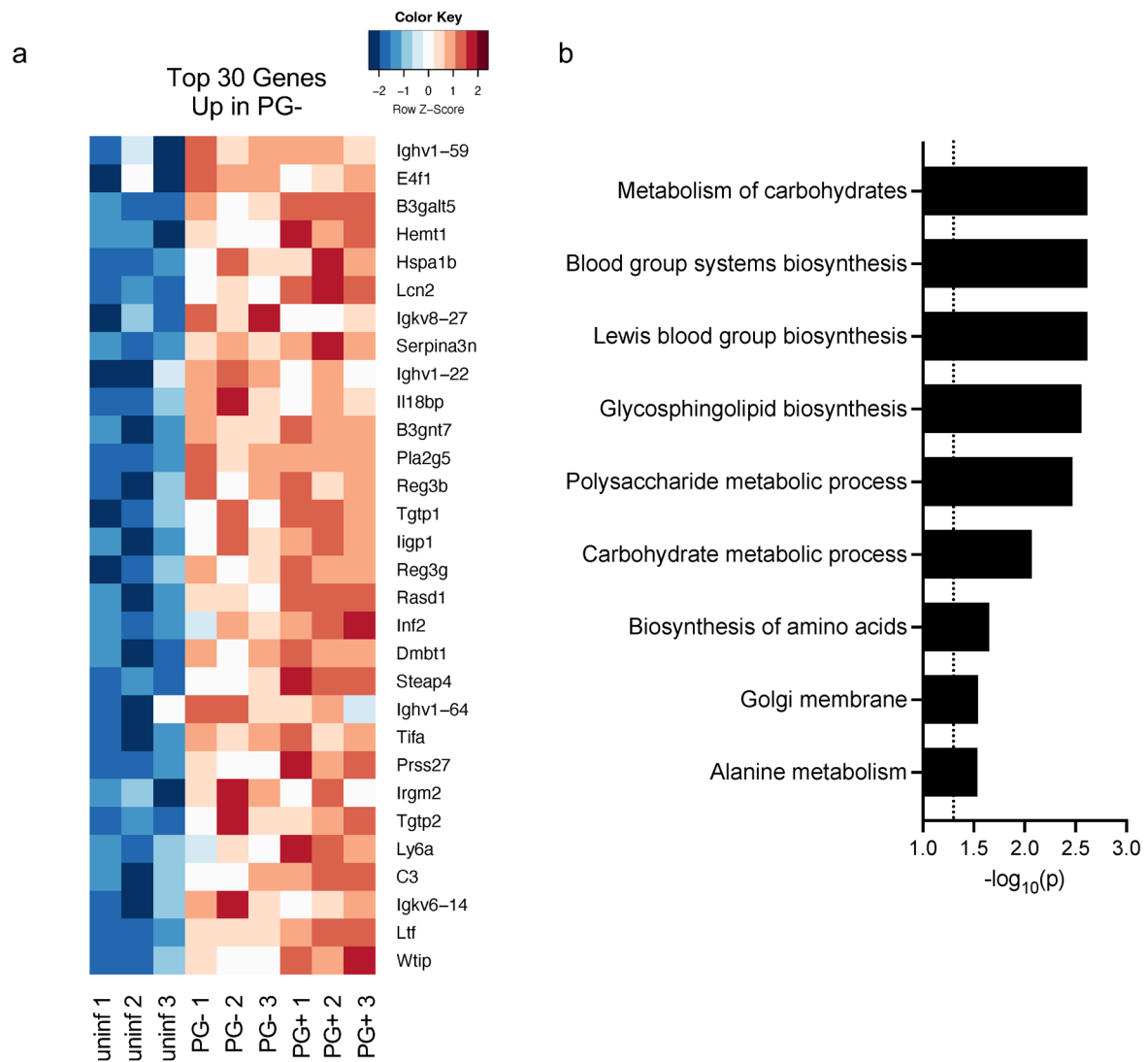
Extended Data Fig. 2 | Non-pyogranuloma tissue does not undergo inflammation. (a) Heat map of top 30 significantly upregulated genes in PG- compared to uninfected samples in descending order by fold change. False discovery rate < 0.05 using Benjamini–Hochberg procedure. (b) Gene ontology analysis of top 30 upregulated genes by fold change only in PG- compared to uninfected samples. Dotted line denotes p = 0.05.
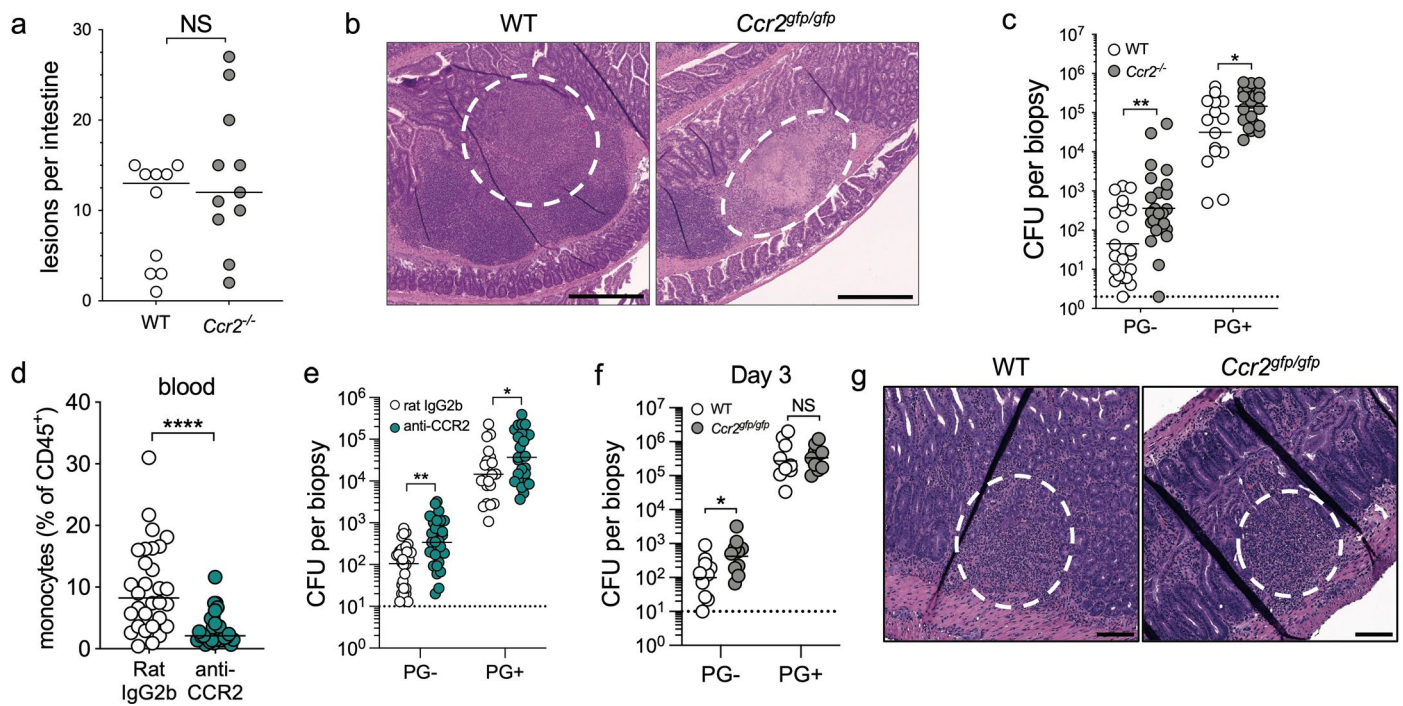
Extended Data Fig. 3 | CCR2-deficient mice cannot control intestinal *Yersinia*.
(**a**) Quantification of total number of intestinal lesions at day 3 post infection. Each data point indicates one mouse (n = 9-11). Line represents median. Pooled from two independent experiments. (**b**) H&E-stained paraffin-embedded small-intestinal sections containing Peyer's patches from WT and *Ccr2gfp/gfp* mice at day 5 post infection. Dashed circle denotes area containing pyogranuloma or necrosuppurative lesion. Scale bars = 500 μm. Representative images from two independent experiments. (**c**) Bacterial burdens in small intestinal PG- and PG + tissue at day 3 post infection. Each data point represents mean CFU of 3-5 pooled punch biopsies from one mouse (n = 15-25). Lines represent geometric mean. Pooled data from four independent experiments. (**d**) Frequency of monocytes in blood at day 5 post infection. Each data point represents one mouse (n = 29-30). Lines indicate median. Pooled data from four independent

experiments. (**e**) Bacterial burdens in small intestinal PG- and PG + tissue at day 5 post infection. Each data point represents the mean CFU of 3-5 pooled punch biopsies from one mouse (n = 21-30). Lines indicate geometric mean. Data pooled from four independent experiments. (**f**) Bacterial burdens in small intestinal PG- and PG + tissue at day 3 post infection. Each data point represents the mean CFU of 3-5 pooled punch biopsies from one mouse (n = 10-13). Lines indicate geometric mean. Pooled data from two independent experiments. (**g**) H&E-stained paraffin-embedded sections containing pyogranulomas from WT and *Ccr2gfp/gfp* mice at day 3 post-infection. Dashed circle denotes area containing pyogranuloma. Scale bars = 100 μm. Representative images of one experiment. All statistical analyses by Mann-Whitney U test (two-tailed). * (p < 0.05), ** (p < 0.01), *** (p < 0.001), **** (p < 0.0001), NS (not significant, p > 0.05).
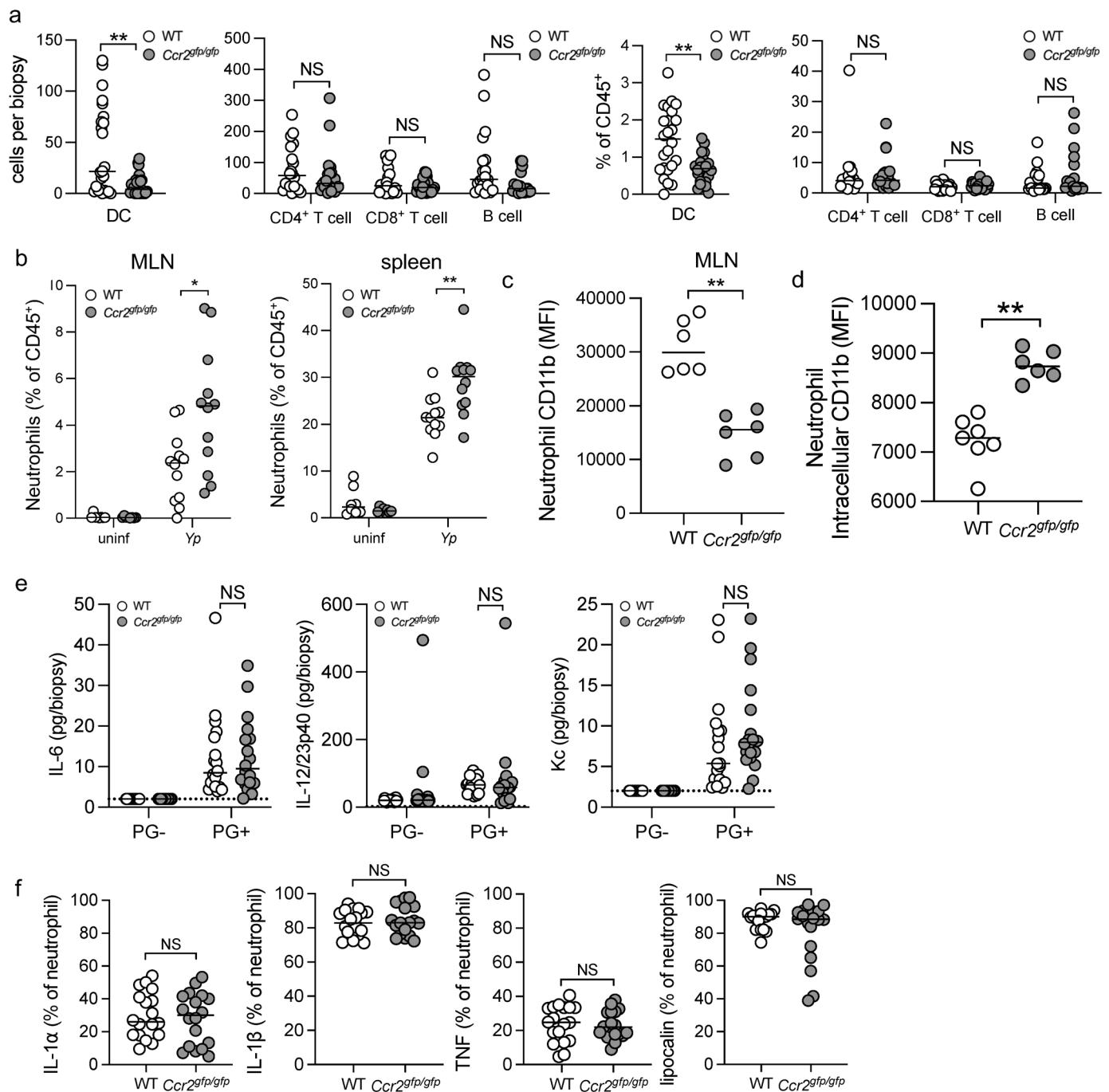
Extended Data Fig. 4 | Effects of monocyte deficiency on other cell types.
(**a**) Total numbers and frequencies of CD4+ T cells, CD8+ T cells, B cells, and DCs in small intestinal PG + tissue. Each data point indicates the mean of 3-10 pooled punch biopsies from one mouse (n = 20-22). Lines represent median. Pooled data from three to five independent experiments. (**b**) Frequency of neutrophils in MLN and spleen at day 5 post infection. Each data point represents one mouse (n = 8-12). Lines represent median. Pooled data from two independent experiments. (**c**) Neutrophil surface CD11b expression in MLN at day 5 post-infection was measured by flow cytometry. Each data point represents one mouse (n = 6). Lines represent median. Representative of two independent experiments. (**d**) Intracellular levels of CD11b in neutrophils in small intestinal PG + tissue at day 5 post-infection were measured by flow cytometry. Each data point represents the mean of 3-10 pooled punch biopsies from one mouse (n = 6-7). Lines represent median. Representative of four independent experiments. (**e**) Cytokine levels in homogenates of tissue punch biopsies at day 5 post infection were measured by cytometric bead array. Each data point represents the mean of 3-10 pooled punch biopsies from one mouse (n = 18-22). Lines represent median. Pooled data from three independent experiments. (**f**) Intracellular levels of cytokines and lipocalin in neutrophils in small intestinal PG + tissue at day 5 post-infection were measured by flow cytometry. Each data point represents the mean of 3-10 pooled punch biopsies from one mouse (n = 18-19). Lines represent median. Pooled data from three independent experiments. All statistical analyses by Mann-Whitney U test (two-tailed). * (p < 0.05), ** (p < 0.01), *** (p < 0.001), **** (p < 0.0001), NS (not significant, p > 0.05).
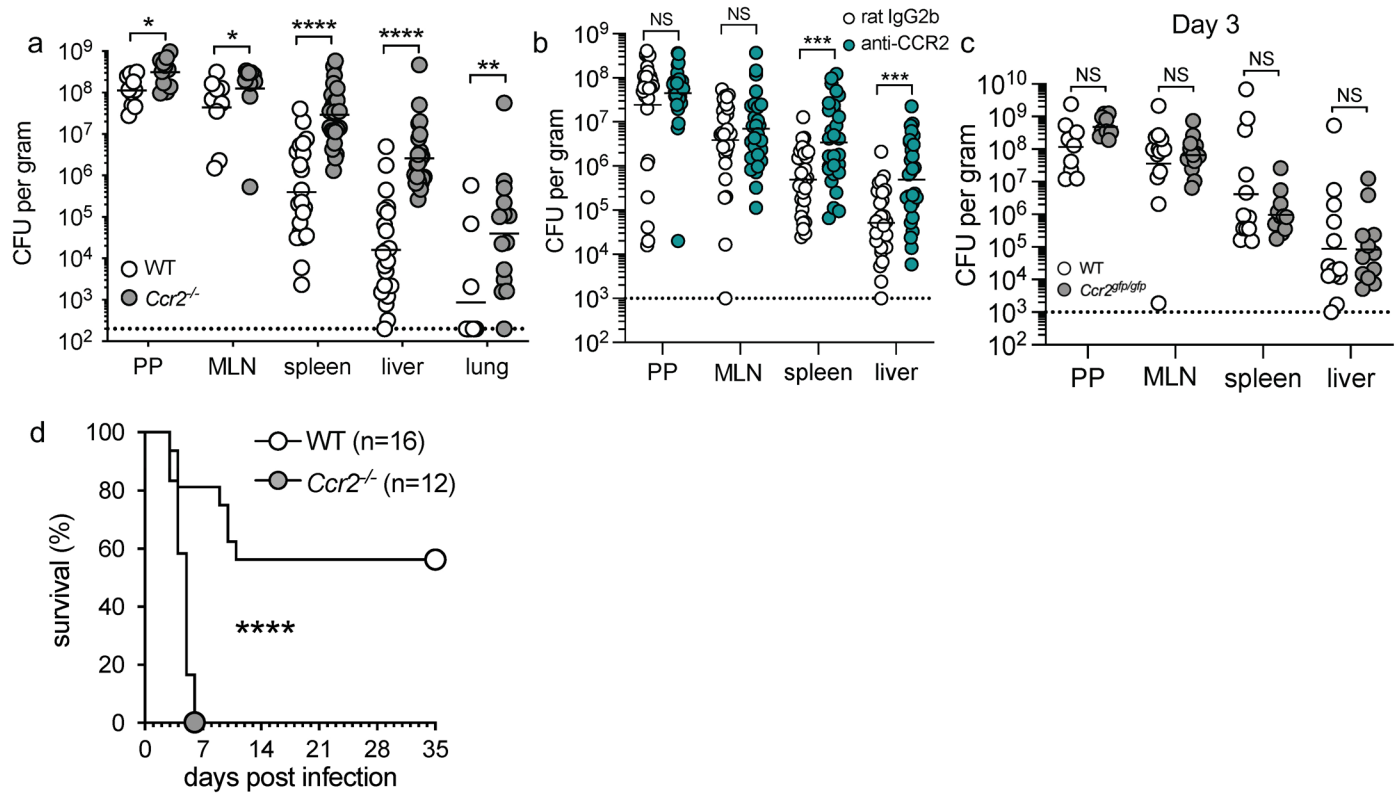
Extended Data Fig. 5 | CCR2-deficient mice cannot control systemic _Yersinia_. (**a**) Bacterial burdens in indicated organs at day 3 post infection. Each data point represents one mouse (n = 10-14 for PP, MLN, lung; 21-25 for spleen, liver). Lines represent geometric mean. Pooled data from two to four independent experiments. (**b**) Bacterial burdens in indicated organs at day 5 post infection. Each data point represents one mouse (n = 29-30). Lines represent geometric mean. Pooled data from four independent experiments. (**c**) Bacterial burdens in indicated organs at day 3 post infection. Each data point represents one mouse (n = 10-13). Lines represent geometric mean. Pooled data from two independent experiments. (**d**) Survival of infected mice. Pooled data from two independent experiments. Statistical analyses by (a-c) Mann-Whitney U test (two-tailed) or (d) Mantel-Cox test. * (p < 0.05), ** (p < 0.01), *** (p < 0.001), **** (p < 0.0001), NS (not significant, p > 0.05).
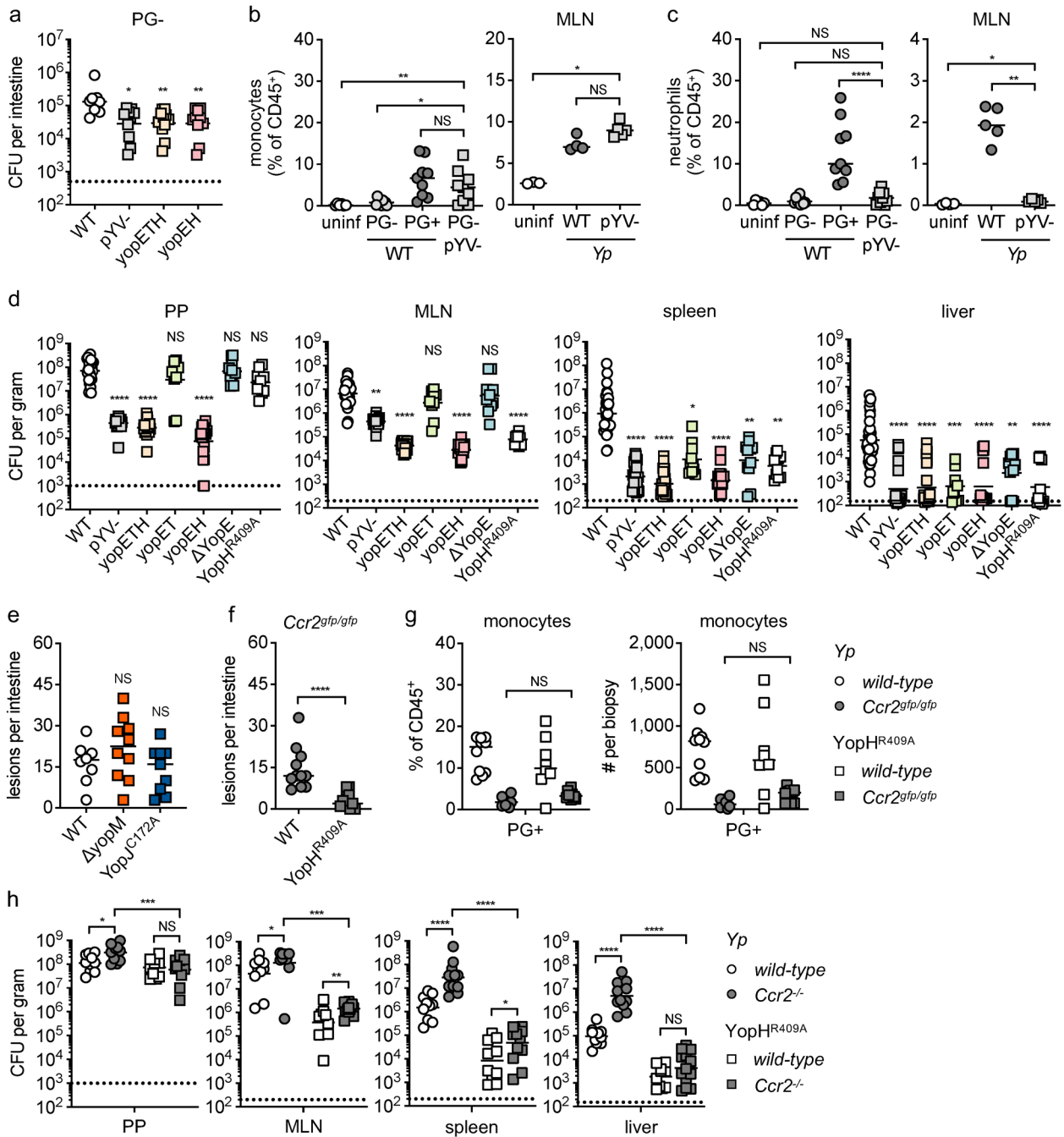
Extended Data Fig. 6 | _Yersinia_ virulence factors induce intestinal pyogranulomas. (**a**) Cumulative bacterial burdens in PG- tissue at day 5 post infection. Each symbol represents one mouse (n = 9-11). Lines represent geometric mean. Dotted line represents limit of detection. Pooled from two independent experiments. (**b**) Frequency of monocytes in small-intestinal tissue and MLN. Each symbol represents one mouse (n = 3-9). Lines represent median. Pooled and representative data from two independent experiments. (**c**) Frequency of neutrophils in small-intestinal tissue and MLN. Each symbol represents one mouse (n = 3-9). Lines represent median. Pooled and representative data from two independent experiments. (**d**) Bacterial burdens in indicated organs at day 5 post-infection. Each symbol represents one mouse (n = 10-43). Lines represent geometric mean. Pooled from 2-6 independent experiments. (**e**) Total number of intestinal lesions at day 5 post infection.

Each symbol represents one mouse (n = 8-10). Lines represent median. Pooled from two independent experiments. (**f**) Total number of intestinal lesions at day 5 post infection. Each symbol represents one mouse (n = 11). Lines represent median. Pooled from three independent experiments. (**g**) Frequency and total number of monocytes in small-intestinal PG + tissue at day 5 post WT or YopH[R409A] _Yp_ infection. Each data point represents one mouse (n = 8-10). Lines represent median. Pooled from two independent experiments. (**h**) Bacterial burdens in indicated organs at day 3 post WT or YopH[R409A] _Yp_ infection. Each symbol represents one mouse (n = 10-13). Lines represent geometric mean. Pooled from two independent experiments. Statistical analyses by (a, d, e) Kruskal–Wallis test with Dunn's post-test and (b, c, f, g, h) Mann-Whitney U test (two-tailed). * (p < 0.05), ** (p < 0.01), *** (p < 0.001), **** (p < 0.0001), NS (not significant, p > 0.05).
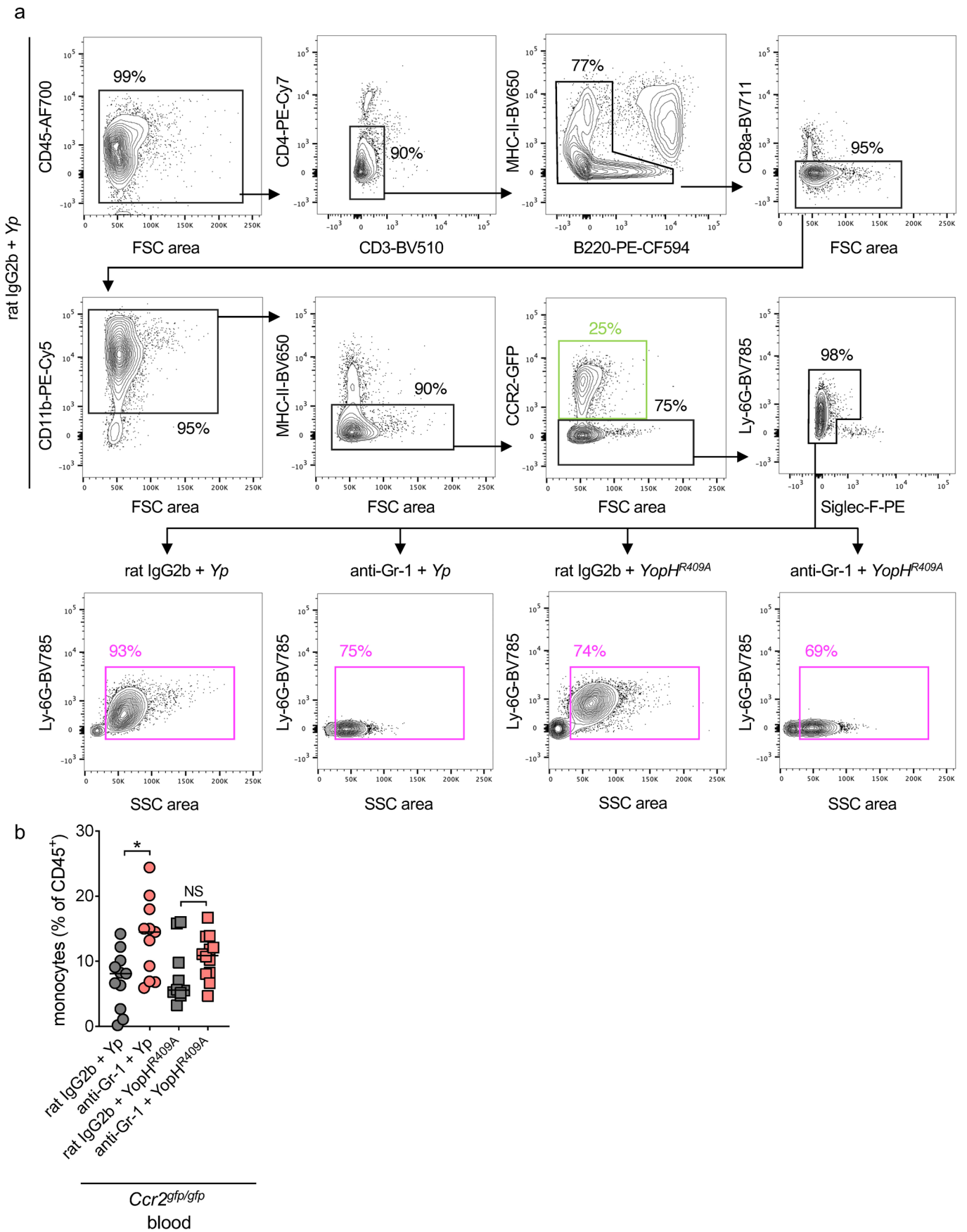
Extended Data Fig. 7 | See next page for caption.

Extended Data Fig. 7 | Anti-Gr-1 effectively depletes neutrophils during infection. (**a**) Flow cytometry plots displaying the gating strategy employed to identify neutrophils and monocytes upon anti-Gr-1 administration. Due to masking of Ly-6G and Ly-6C epitopes by anti-Gr-1, monocytes were identified as CCR2-GFP⁺ cells (green box) and neutrophils were identified as SSC high cells (pink boxes). Representative images of three independent experiments.

(**b**) Frequency of monocytes in blood at day 5 post infection was determined by flow cytometry. Each symbol represents one mouse (n = 10-11). Lines represent median. Data from three independent experiments. Statistical analyses by Kruskal-Wallis test with Dunn's post-test. * (p < 0.05), ** (p < 0.01), *** (p < 0.001), **** (p < 0.0001), NS (not significant, p > 0.05).

Corresponding author(s): Igor E. Brodsky

Last updated by author(s): Feb 2, 2023

Reporting Summary

Nature Portfolio wishes to improve the reproducibility of the work that we publish. This form provides structure for consistency and transparency in reporting. For further information on Nature Portfolio policies, see our Editorial Policies and the Editorial Policy Checklist.

Statistics

For all statistical analyses, confirm that the following items are present in the figure legend, table legend, main text, or Methods section.

n/a	Confirmed	
☐	☒	The exact sample size (*n*) for each experimental group/condition, given as a discrete number and unit of measurement
☐	☒	A statement on whether measurements were taken from distinct samples or whether the same sample was measured repeatedly
☐	☒	The statistical test(s) used AND whether they are one- or two-sided *Only common tests should be described solely by name; describe more complex techniques in the Methods section.*
☒	☐	A description of all covariates tested
☐	☒	A description of any assumptions or corrections, such as tests of normality and adjustment for multiple comparisons
☐	☒	A full description of the statistical parameters including central tendency (e.g. means) or other basic estimates (e.g. regression coefficient) AND variation (e.g. standard deviation) or associated estimates of uncertainty (e.g. confidence intervals)
☐	☒	For null hypothesis testing, the test statistic (e.g. *F*, *t*, *r*) with confidence intervals, effect sizes, degrees of freedom and *P* value noted *Give P values as exact values whenever suitable.*
☒	☐	For Bayesian analysis, information on the choice of priors and Markov chain Monte Carlo settings
☒	☐	For hierarchical and complex designs, identification of the appropriate level for tests and full reporting of outcomes
☒	☐	Estimates of effect sizes (e.g. Cohen's *d*, Pearson's *r*), indicating how they were calculated

Our web collection on statistics for biologists contains articles on many of the points above.

Software and code

Policy information about availability of computer code

Data collection	FACSDiva v9.0, Illumina NextSeq 500
Data analysis	Prism v9.0, FlowJo v10, ImageJ v2.1, Kallisto v0.46.2, R v4.0.3, RStudio v1.2.5042, Bioconductor

For manuscripts utilizing custom algorithms or software that are central to the research but not yet described in published literature, software must be made available to editors and reviewers. We strongly encourage code deposition in a community repository (e.g. GitHub). See the Nature Portfolio guidelines for submitting code & software for further information.

Data

Policy information about availability of data

All manuscripts must include a data availability statement. This statement should provide the following information, where applicable:
- Accession codes, unique identifiers, or web links for publicly available datasets
- A description of any restrictions on data availability
- For clinical datasets or third party data, please ensure that the statement adheres to our policy

Raw RNA sequencing data are available on the Gene Expression Omnibus (GEO; accession no. GSE194334). All other raw data are available upon request to the corresponding author.

Human research participants

Reporting on sex and gender	The study contains no human subjects
Population characteristics	The study contains no human subjects
Recruitment	The study contains no human subjects
Ethics oversight	The study contains no human subjects

Note that full information on the approval of the study protocol must also be provided in the manuscript.

Field-specific reporting

Please select the one below that is the best fit for your research. If you are not sure, read the appropriate sections before making your selection.

☒ Life sciences   ☐ Behavioural & social sciences   ☐ Ecological, evolutionary & environmental sciences

For a reference copy of the document with all sections, see nature.com/documents/nr-reporting-summary-flat.pdf

Life sciences study design

All studies must disclose on these points even when the disclosure is negative.

Sample size	To determine experimental animal group sizes and account for experimental variability associated with in vivo experiments, power analysis was performed on previous published data sets involving animal studies in the lab (Brodsky et al., Cell Host Microbe, 2010; Philip et al., PNAS 2014; Peterson et al., JI 2016; Peterson et al. JEM 2017). For the following parameters: cytokine responses, flow cytometry, bacterial burdens and bacterial-induced inflammation, it was calculated that groups of five animals were required for statistical differences ($p < 0.05$; Power > 0.8) to be observed between groups.
Data exclusions	No data were excluded from analysis.
Replication	Experiments were successfully repeated two to six times to ensure reproducibility of results.
Randomization	All mice were randomly assigned to treatment groups. We do not observe a sex-specific phenotype. Nevertheless, male and female mice were randomly assigned to treatment groups.
Blinding	Samples were assigned numbers without revealing treatment group. Data collection and analyses were conducted in a blinded manner.

Reporting for specific materials, systems and methods

We require information from authors about some types of materials, experimental systems and methods used in many studies. Here, indicate whether each material, system or method listed is relevant to your study. If you are not sure if a list item applies to your research, read the appropriate section before selecting a response.

Materials & experimental systems

n/a	Involved in the study
☐	☒ Antibodies
☒	☐ Eukaryotic cell lines
☒	☐ Palaeontology and archaeology
☐	☒ Animals and other organisms
☒	☐ Clinical data
☒	☐ Dual use research of concern

Methods

n/a	Involved in the study
☒	☐ ChIP-seq
☐	☒ Flow cytometry
☒	☐ MRI-based neuroimaging

Antibodies

Antibodies used	Rat anti-mouse CCR2 (clone MC-21 AK; Matthias Mack, University Hospital Regensburg), rat anti-mouse Ly-6G (1A8; Bio X Cell), anti-rat kappa Ig light chain (MAR 18.5; Bio X Cell), rat anti-mouse Gr-1 (RB6-8C5; Bio X Cell), PE-conjugated rat anti-mouse Siglec-F (E50-2440; BD Biosciences), PE-TxR or PE-Cy5-conjugated rat anti-mouse CD11b (M1/70.15; Thermo Fisher Scientific), PE-Cy5-

conjugated mouse anti-mouse NK1.1 (PK136; BioLegend), PE-Cy5.5 or PE-Cy7-conjugated rat anti-mouse CD4 (RM4-5; Thermo Fisher Scientific), PE-Cy7-conjugated rat anti-mouse CD3 (17A2; BioLegend), BV510-conjugated rat anti-mouse CD3e (145-2C11; BioLegend), FITC-conjugated Armenian hamster anti-mouse CD11c (N418; BioLegend), PerCP-Cy5.5-conjugated rat anti-mouse Ly-6C (HK1.4; Thermo Fisher Scientific), PB-conjugated rat anti-mouse CD90.2 (53-2.1; BioLegend), BV510-conjugated rat anti-mouse CD19 (1D3; BD Biosciences), BV605-conjugated Armenian hamster anti-mouse TCRβ (H57-597; BD Biosciences), BV650-conjugated rat anti-mouse I-A/I-E (M5/114.15.2; BD Biosciences), BV711-conjugated rat anti-mouse CD8α (53-6.7; BD Biosciences), BV785-conjugated rat anti-mouse Ly-6G (1A8; Thermo Fisher Scientific), AF647-conjugated mouse anti-mouse CD64 (X54-5/7.1; BD Biosciences), AF700-conjugated mouse anti-mouse CD45.2 (104; BioLegend), PE-CF594-conjugated rat anti-mouse CD45R/B220 (RA3-6B2; BD Biosciences).

| Validation | All commercial antibodies have been validated by the manufacturer. The anti-CCR2 antibody was experimentally validated in cell lines overexpressing CCR2 and on primary mouse cells (Mack et al. JI 2001). |

Animals and other research organisms

Policy information about studies involving animals; ARRIVE guidelines recommended for reporting animal research, and Sex and Gender in Research

Laboratory animals	C57BL/6 wild-type mice (Mus musculus) were used for this study along with Ccr2gfp/gfp and Ccr2-/- mice between the ages of 8-12 weeks. Mice were housed at 20-26°C, with relative humidity 30-70, and were maintained on a 12/12-hour light/dark cycle.
Wild animals	The study did not involve wild animals.
Reporting on sex	Mice do not exhibit sex-specific responses to Yersinia infection and have therefore not been segregated. Thus, all experiments were conducted using both male and female mice (1:1), which were randomly assigned to treatment groups.
Field-collected samples	The study did not involved samples collected from the field.
Ethics oversight	University of Pennsylvania Institutional Animal Care and Use Committee

Note that full information on the approval of the study protocol must also be provided in the manuscript.

Flow Cytometry

Plots

Confirm that:

☒ The axis labels state the marker and fluorochrome used (e.g. CD4-FITC).

☒ The axis scales are clearly visible. Include numbers along axes only for bottom left plot of group (a 'group' is an analysis of identical markers).

☒ All plots are contour plots with outliers or pseudocolor plots.

☒ A numerical value for number of cells or percentage (with statistics) is provided.

Methodology

| Sample preparation | Blood was harvested by cardiac puncture upon euthanasia and collected in 250 U/ml Heparin solution (Millipore Sigma) prior to erythrocyte lysis with Red Blood Cell Lysing Buffer (Millipore Sigma).

Lymph nodes and spleens were homogenized through a 70 µm cell strainer (Fisher Scientific), then flushed with R10 buffer consisting of RPMI 1640 (Millipore Sigma) supplemented with 10 mM HEPES (Millipore Sigma), 10% fetal bovine serum (Omega Scientific), 1 mM sodium pyruvate (Thermo-Fisher Scientific) and 100 U/ml penicillin + 100 µg/ml streptomycin (Thermo Fisher Scientific).

Intestines were excised, flushed luminally with sterile PBS to remove the feces, opened longitudinally along the mesenteric side and placed luminal side down on cutting boards (Epicurean). Small-intestinal tissue containing macroscopically visible pyogranulomas (PG+), adjacent non-granulomatous areas (PG-) and uninfected control tissue (uninf) were excised using a 2 mm-ø dermal punch-biopsy tool (Keyes). Biopsies within each mouse were pooled groupwise, suspended in epithelial-dissociation buffer consisting of calcium and magnesium-free HBSS (Thermo Fisher Scientific) supplemented with 15 mM HEPES, 10 mg/ml bovine serum albumin (Millipore Sigma), 5 mM EDTA (Millipore Sigma) and 100 U/ml penicillin + 100 µg/ml streptomycin, then incubated for 30 minutes at 37°C under continuous agitation. To isolate immune cells from the lamina propria, the tissue was enzymatically digested in R10 buffer, along with 0.5 Wünsch units/ml liberase TM (Roche), 30 µg/ml DNase I (Roche), and 5 mM CaCl2 for 20 min at 37°C under continuous agitation. The resulting cell suspensions were filtered through 100 µm cell strainers (Fisher Scientific) and subjected to density-gradient centrifugation using Percoll (GE Healthcare). Briefly, cells were suspended in 40% Percoll and centrifuged over a 70% Percoll layer for 20 min at 600 × g with lowest brake at room temperature. Cells collected between the layers were washed with R10 for downstream analysis.

Unspecific Fc binding was blocked for 10 minutes on ice with unconjugated anti-CD16/CD32 (93; Thermo-Fisher Scientific). Cells were subsequently fluorescently labeled for 30 minutes on ice with the following antibodies and reagents: PE-conjugated rat anti-mouse Siglec-F (E50-2440; BD Biosciences), PE-TxR or PE-Cy5-conjugated rat anti-mouse CD11b (M1/70.15; Thermo Fisher Scientific), PE-Cy5-conjugated mouse anti-mouse NK1.1 (PK136; BioLegend), PE-Cy5.5 or PE-Cy7-conjugated rat anti-mouse CD4 (RM4-5; Thermo Fisher Scientific), PE-Cy7-conjugated rat anti-mouse CD3 (17A2; BioLegend), |

BV510-conjugated rat anti-mouse CD3e (145-2C11; BioLegend), FITC-conjugated Armenian hamster anti-mouse CD11c (N418; BioLegend), PerCP-Cy5.5-conjugated rat anti-mouse Ly-6C (HK1.4; Thermo Fisher Scientific), PB-conjugated rat anti-mouse CD90.2 (53-2.1; BioLegend), BV510-conjugated rat anti-mouse CD19 (1D3; BD Biosciences), BV605-conjugated Armenian hamster anti-mouse TCRβ (H57-597; BD Biosciences), BV650-conjugated rat anti-mouse I-A/I-E (M5/114.15.2; BD Biosciences), BV711-conjugated rat anti-mouse CD8α (53-6.7; BD Biosciences), BV785-conjugated rat anti-mouse Ly-6G (1A8; Thermo Fisher Scientific), AF647-conjugated mouse anti-mouse CD64 (X54-5/7.1; BD Biosciences), AF700-conjugated mouse anti-mouse CD45.2 (104; BioLegend), PE-CF594-conjugated rat anti-mouse CD45R/B220 (RA3-6B2; BD Biosciences) along with eF780 viability dye (BioLegend) diluted in PBS. Antibodies were used at 1:200 dilution and viability dye at 1:1500 dilution.

For intracellular staining, cells were incubated for 3 hours at 37°C with 5% CO2 in R10 buffer supplemented with 0.33 μl/ml GolgiStop (BD Biosciences) and 15 μg/ml DNase I. Surface proteins were stained as above, then cells were fixed for 20 minutes on ice with Cytofix/Cytoperm Fixation/ Permeabilization solution (BD Biosciences). Lipocalin-2 was stained using biotin-conjugated rat anti-mouse lipocalin-2 (NGAL; BioLegend) on ice for one hour followed by BV711-conjugated streptavidin (BD Biosciences) at 4°C overnight. Intracellular cytokines were stained at 4°C overnight with PerCP-e710-conjugated rat anti-mouse IL-1β (NJTEN3; Thermo Fisher Scientific), eF450-conjugated rat anti-mouse TNF (MP6-XT22; Thermo Fisher Scientific), PE-conjugated Armenian hamster anti-mouse IL-1? (ALF-161; BioLegend). All intracellular antibodies were diluted 1:200 in Perm/Wash Buffer (BD Biosciences). Streptavidin was diluted 1:400 in Perm/Wash Buffer. Cells were acquired on an LSRFortessa flow cytometer with FACSDiva v9.0 and data was analyzed with FlowJo v10. Dead and clustered cells were removed from all analyses.

Instrument: BD LSRFortessa.

Software: BD FACSDiva v9.0 and FlowJo v10.8.1 were used for collection and analysis, respectively.

Cell population abundance: No cells were sorted for this study.

Gating strategy: Diagrams are provided in Extended Data Fig. 1a and 7a.

☒ Tick this box to confirm that a figure exemplifying the gating strategy is provided in the Supplementary Information.